



Direct numerical simulation of turbulence over resolved and modeled rough walls with irregularly distributed roughness

メタデータ	言語: eng 出版者: 公開日: 2020-10-27 キーワード (Ja): キーワード (En): 作成者: Kuwata, Yusuke, Kawaguchi, Yasuo メールアドレス: 所属:
URL	http://hdl.handle.net/10466/00017113

Direct Numerical Simulation of Turbulence over Resolved and Modeled Rough Walls with Irregularly Distributed Roughness

Y. Kuwata^{a,*}, Y. Kawaguchi^b

^a*Department of Mechanical Engineering, Osaka Prefecture University, 1-1 Sakai, Osaka 599-8531, Japan*

^b*Department of Mechanical Engineering, Tokyo University of Science, 2641 Yamazaki, Noda, Chiba 278-8510, Japan*

Abstract

To simulate turbulent flow over a rough wall without resolving complicated rough geometries, a macroscopic rough wall model is developed based on spatial (plane) averaging theory. The plane-averaged drag force term, which arises through averaging the Navier-Stokes equations in a plane parallel to a rough wall, can be modeled using a plane porosity and a plane hydraulic diameter. To evaluate the developed model, direct and macroscopic model simulations for turbulence over irregularly distributed semi-spheres at Reynolds number of 300 are carried out using the D3Q27 multiple-relaxation time lattice Boltzmann method. The results show that the developed model can be used to predict rough wall skin friction. The results agree quantitatively with standard turbulence statistics such as mean velocity and Reynolds stress profiles with the fully resolved DNS data. Since velocity dispersion occurs inside the rough wall and is found to contribute to turbulence energy dissipation,

*corresponding author

Email address: `kuwata@me.osakafu-u.ac.jp` (Y. Kuwata)

which the developed model cannot account for, the developed model fails to reproduce dispersion-related turbulence energy dissipation. However, it is found that the plane-averaged drag force term can successfully recover the deficiency of dispersion-related turbulence energy dissipation.

Keywords: Direct numerical simulation, Rough wall turbulence, Lattice Boltzmann method, Macroscopic rough wall model

1. Introduction

In most geophysical and engineering flows, the underlying surface is hydraulically rough. From a geophysical perspective, flows over vegetated and urban canopies, and natural river beds can be classified as rough wall turbulence (Raupach, 1994; Finnigan, 2000; Cheng and Castro, 2002). Furthermore, wall roughness inevitably occurs in engineering devices due to imperfections in production processes, erosion or corrosion by aging, and organic or inorganic fouling processes, which significantly increase friction, especially in turbulent flow with high Reynolds number (Wahl, 1989; Bons et al., 2001; Langelandsvik et al., 2008; Kirschner and Brennan, 2012). Hence, it is readily recognized that predicting the influence of wall roughness on turbulence is crucial in engineering design, meteorological, and geological applications.

The most important effect of wall roughness on turbulent flows is the downward shift in the mean velocity profile, known as the roughness function, which is a consequent modification of friction factor (Hama, 1954; Schlichting et al., 1960). The pioneering work on this effect was performed by Nikuradse (1933). His large number of measurements of a pressure drop in pipes with walls covered by sand grains revealed that the friction fac-

tor only depended on an equivalent sand roughness in a sufficiently high Reynolds number regime, and a logarithmic velocity profile could still be used in the outer layer. Further extensions of this work was performed by Colebrook et al. (1939), who investigated the friction factor for several industrial pipes. Moody (1944) consolidated those data as a Moody chart for practical engineering applications. The Moody chart is certainly a powerful tool for estimating the friction factor in roughened pipes. However, an equivalent roughness is required in order to read a friction factor from the Moody chart, thus application of the Moody chart is limited to rough surfaces whose equivalent wall roughness is known a priori. Applicable examples include commercial steel pipes, glass, and concrete, while applying readings from a Moody chart to naturally occurring roughness with unknown equivalent roughness is very challenging.

Accordingly, many studies have dedicated their efforts to determining the equivalent roughness (Schlichting et al., 1960; Dvorak, 1969; Dirling, 1973; Coleman et al., 1984; Sigal and Danberg, 1990; Van Rij et al., 2002). Dirling (1973) proposed a roughness parameter that includes a roughness density and a shape parameter. The roughness density represents the solidity of roughness elements, while the shape parameter accounts for the frontal area and the windward wetted surface area of a single roughness element. This roughness parameter was further extended and examined by Sigal and Danberg (1990); Van Rij et al. (2002) by introducing ratio of the smooth surface area before adding roughness to the total frontal area over rough surfaces. Van Rij et al. (2002) reported that the proposed procedure could be also applicable to walls with non-uniform, three-dimensional roughness with ir-

regular geometry and arrangement. Although several roughness parameters for determining the equivalent roughness have been examined, applying these to complex, irregular rough walls is not always straightforward. A correlation function based on statistical moments of surface elevation with the equivalent roughness have been explored recently (Musker, 1980; Townsin et al., 1981; Flack and Schultz, 2010). It was reported by Flack and Schultz (2010) that the root-mean-square roughness height and the skewness of surface elevation were the most effective parameters in describing a surface hydraulically. A review of hydraulic roughness parameters for determining the equivalent roughness was given by Flack and Schultz (2010).

Many other roughness parameters for determining the equivalent roughness were discussed in terms of a large amount of experimental data. However, most of them are based on empirical or phenomenological discussions due to the difficulty in measuring flows near rough walls. Hence, fundamental discussions on rough wall turbulence were primarily investigated using direct numerical simulations (DNS) or large eddy simulations (LES) with fully resolved rough walls, e.g., simulations over spanwise extended transverse ribs (Miyake et al., 2001; Leonardi et al., 2003; Ashrafian et al., 2004; Ikeda and Durbin, 2007; Jin et al., 2015), three dimensional roughness (Bhaganagar et al., 2004; Orlandi and Leonardi, 2008; Lee et al., 2011; Chatzikyriakou et al., 2015; Kuwata and Suga, 2016b,c), or random roughness (Napoli et al., 2008; Cardillo et al., 2013; Busse et al., 2015). However, since turbulent simulations with fully resolved roughness elements require fine grids to resolve small scale turbulence proximate to the roughness elements and large computational domain enough to capture large-scale turbulence structures, DNS

of turbulent flows over complex rough walls such as moving plant canopies is still beyond the power of modern supercomputers (Busse and Sandham, 2012).

In contrast to simulations with fully resolved roughness, simulations with models or virtual rough walls are effective for predicting flows, saving considerable computational costs and revealing the nature of rough wall turbulence. A most simple approach to model rough walls is by modifying a wall boundary condition (Tuck and Kouzoubov, 1995; Jäger and Mikelić, 2001; Orlandi et al., 2003; Flores and Jimenez, 2006). Orlandi et al. (2003) carried out DNS of turbulent channel flows with non-zero wall velocity disturbance. It was reported that drag reduction occurred over the wall with the longitudinal velocity disturbance, while the turbulence structure over the wall with the wall-normal velocity disturbance was similar to those observed over the rough wall turbulence, resulting in increased drag. They concluded that the characteristics of rough wall turbulence reflected the presence of a non-zero wall-normal velocity disturbance at the interface of rough walls.

Another way to reproduce rough wall turbulence is by adding an external force term to the Navier-Stokes equations (Miyake et al., 2000; Scotti, 2006; Breugem et al., 2006; Busse and Sandham, 2012). Miyake et al. (2000) introduced a Stokes drag force to model the influence of rough walls. They reported that the predicted roughness function due to an increased friction factor was qualitatively comparable to the experimental data. Furthermore, they also reported that disappearing or reduction in thickness of a viscous sublayer could be reproduced with the proposed model, which is known to occur experimentally. Busse and Sandham (2012) also introduced an extra force

term that contained a roughness density, wall-roughness height, and shape function of distance from a channel wall. They confirmed that turbulence statistics over the modeled rough wall showed good qualitative agreement with the experimental data based on simulations with a large number of parameter combinations, and the model could successfully reproduce several features of turbulence near a rough wall. However, they commented that the model must be carefully calibrated against experiments or rough wall resolved DNS for use in practical applications. In a similar way but with a more theoretical approach, Breugem et al. (2006) added a term with a spatial derivative of porosity and an external drag force, which were theoretically derived using spatial (volume) averaging theory (Whitaker, 1986, 1996). Their simulation results including turbulence structures and turbulence statistics were qualitatively consistent with experimental observations.

Although many other important attempts were made to model rough wall turbulence, nearly all the models in the literature ignored or treated unknown correlations without rigorous validation against fully resolved DNS. The aim of this study is to develop a more elaborate rough wall model based on the spatial averaging theory with a rigorous validation against DNS of fully resolved roughness. Furthermore, a discussion on the underlying physics of the wall turbulence was attempted by analyzing momentum and turbulent transport budget terms.

Nomenclature

A_S : plane area of a representative elementary plane

A_{S_f} : plane area of the fluid phase contained within a representative elementary plane

c : particle velocity: $c = \Delta/\delta t$

c_s : speed of sound: $c_s/c = 1/\sqrt{3}$

C_f : Skin friction coefficient

C_1^D, C_2^D : model coefficients in the plane-averaged drag force model

D_m : plane hydraulic diameter

f_i : plane-averaged drag force

\boldsymbol{f} : distribution function

\boldsymbol{f}^{eq} : equilibrium distribution function

\boldsymbol{F} : external force term

g_i^φ : inhomogeneous correction term

h_{max} : maximum height of a rough wall

h_m : mean height of a rough wall

h_{rms} : standard deviation of roughness elevation

k : macro-scale turbulence energy: $k = R_{kk}/2$

k^A : plane-averaged turbulence energy: $k^A = R_{kk}^A/2$

ℓ : circumference length of solid obstacles

L_x : streamwise length of the computational domain

L_y : wall-normal length of the computational domain

L_z : spanwise length of the computational domain

\mathbf{M} : transformation matrix

p : pressure

r_{ij} : micro-scale Reynolds stress: $\overline{\varphi \langle \tilde{u}'_i \tilde{u}'_j \rangle^f}$

R_{ij} : macro-scale Reynolds stress: $\overline{\varphi \langle u'_i \rangle^f \langle u'_j \rangle^f}$

R_{ij}^A : plane-averaged Reynolds stress: $\overline{\varphi \langle u'_i u'_j \rangle^f}$

Re_τ : friction Reynolds number: $\text{Re}_\tau = u_\tau \delta / \nu$

Sk : skewness of roughness elevation

t : time

u_i : velocity

u_τ : averaged friction velocity at the rough wall

U_b : bulk mean velocity

w_α : weight parameter

x : streamwise coordinate

y : wall-normal coordinate

z : spanwise coordinate

δ : boundary layer thickness

Δ : grid spacing

ΔU : roughness function

ν : kinematic viscosity

τ_{ij} : subfilter-scale stress: $\tau_{ij} = \varphi \langle \tilde{u}_i \tilde{u}_j \rangle^f$

ξ_α : discrete velocity

ρ : fluid density

φ : plane porosity: $\varphi = A_{S_f}/A_s$

ϕ : variable

ω : superficial plane-averaged vorticity: $\omega = \varphi \langle \nabla \times \mathbf{u} \rangle^f$

$\overline{\phi}$: Reynolds averaged value of ϕ

ϕ' : temporal fluctuation of ϕ : $\phi - \overline{\phi}$

$\langle \phi \rangle^f$: intrinsic plane-averaged value of ϕ

$\langle \phi \rangle$: superficial plane-averaged value of ϕ

$()^+$: values normalized by the averaged friction velocity at the rough wall

2. Numerical approach

Since the lattice Boltzmann method (LBM) allows us to accurately treat a curved boundary with simple algorithms, the LBM was recognized as a powerful tool for treating flows in complicated geometries (e.g., Hatiboglu and Babadagli, 2008; Suga et al., 2009; Suga and Nishio, 2009; Beugre et al., 2010; Parmigiani et al., 2011; Chukwudozie and Tyagi, 2013). Owing to this advantage, it has been often applied to various complex turbulent flow problems, such as flows in porous media (e.g., Hasert et al., 2011; Krafczyk et al., 2015; Kuwata and Suga, 2015b, 2016c) or over rough walls (e.g., Jin et al., 2015; Tóth and Jánosi, 2015; Kuwata and Suga, 2016b, 2017). In addition, since the accuracy of the LBM for turbulent flow was recently confirmed from lattice Boltzmann DNS studies (e.g., Lammers et al., 2006; Chikatarla et al., 2010; Bepalko et al., 2012; Suga et al., 2015; Fattahi et al., 2016; Wang et al., 2016; Gehrke et al., 2017), the present study uses the LBM to solve flows over a rough wall. The lattice Boltzmann equation can be obtained by discretizing the velocity space of the Boltzmann equation into a finite number of discrete velocities $\xi_\alpha \{\alpha = 0, \dots, Q - 1\}$. Although there are several discrete velocity models for three-dimensional flow simulations, e.g., the D3Q15, D3Q19 and D3Q27 models, we chose the D3Q27 model because unphysical spurious currents can be reduced with this model (Kuwata and Suga, 2015a). Applying the multiple-relaxation-time (MRT) scheme is effective for ensuring numerical stability in high Reynolds number flow simulations (d’Humières et al., 2002). Hence, we used the D3Q27 MRT-LBM of Suga et al. (2015) for our numerical scheme in this study. The time evolution

of the distribution function in the MRT-LBM can be written as

$$\begin{aligned} |\mathbf{f}(\mathbf{x} + \boldsymbol{\xi}_\alpha \delta t, t + \delta t)\rangle - |\mathbf{f}(\mathbf{x}, t)\rangle = & - \mathbf{M}^{-1} \hat{\mathbf{S}} [|\mathbf{m}(\mathbf{x}, t)\rangle - |\mathbf{m}^{eq}(\mathbf{x}, t)\rangle] \\ & + \mathbf{M}^{-1} \left(\mathbf{I} - \frac{\hat{\mathbf{S}}}{2} \right) \mathbf{M} |\mathbf{F}\rangle \delta t, \end{aligned} \quad (1)$$

where $|\mathbf{f}\rangle$ is $|\mathbf{f}\rangle = (f_0, f_1, \dots, f_{Q-1})^T$ and δt is the time step. Note that $Q = 27$ in the D3Q27 model. The parameters for the D3Q27 model are listed in Table 1. The matrix \mathbf{I} is an identity matrix, and the matrix \mathbf{M} is a $Q \times Q$ matrix which linearly transforms the distribution functions to the moments as follows: $|\mathbf{m}\rangle = \mathbf{M}|\mathbf{f}\rangle$. The equilibrium moment \mathbf{m}^{eq} is $|\mathbf{m}^{eq}\rangle = \mathbf{M}|\mathbf{f}^{eq}\rangle$, with

$$f_\alpha^{eq} = w_\alpha \left(\rho + \rho_0 \left[\frac{\boldsymbol{\xi}_\alpha \cdot \mathbf{u}}{c_s^2} + \frac{(\boldsymbol{\xi}_\alpha \cdot \mathbf{u})^2 - c_s^2 |\mathbf{u}|^2}{2c_s^4} \right] \right), \quad (2)$$

where \mathbf{u} is the fluid velocity and ρ is the sum of constant and fluctuation values: $\rho = \rho_0 + \delta\rho$ (He and Luo, 1997). The speed of sound is $c_s/c = 1/\sqrt{3}$ with $c = \Delta/\delta t$, where Δ is the lattice spacing and the w_α values are listed in Table 1. The equilibrium moments and the transformation matrix are shown in Tables 2 and 3, respectively. Note that there are a few typos to be corrected in terms of the equilibrium moments and the transformation matrix in the original paper by Suga et al. (2015), and the corrected values are shown in Tables 2 and 3.

The collision matrix $\hat{\mathbf{S}}$ is diagonal:

$$\begin{aligned} \hat{\mathbf{S}} \equiv \text{diag}(0, 0, 0, 0, s_4, s_5, s_5, s_7, s_7, s_7, s_{10}, s_{10}, s_{10}, s_{13}, \\ s_{13}, s_{13}, s_{16}, s_{17}, s_{18}, s_{18}, s_{20}, s_{20}, s_{20}, s_{23}, s_{23}, s_{23}, s_{26}). \end{aligned} \quad (3)$$

The relaxation parameters are

$$\begin{aligned} s_4 = 1.54, \quad s_5 = s_7, \quad s_{10} = 1.5, \quad s_{13} = 1.83, \quad s_{16} = 1.4, \\ s_{17} = 1.61, \quad s_{18} = s_{20} = 1.98, \quad s_{23} = s_{26} = 1.74. \end{aligned} \quad (4)$$

The relaxation parameters s_5 and s_7 are related to the kinematic viscosity ν as follows:

$$\nu = c_s^2 \left(\frac{1}{s_5} - \frac{1}{2} \right) \delta t = c_s^2 \left(\frac{1}{s_7} - \frac{1}{2} \right) \delta t. \quad (5)$$

The term \mathbf{F} is the external force term (Guo et al., 2002):

$$F_\alpha = w_\alpha \rho_0 \left\{ \frac{\boldsymbol{\xi}_\alpha \cdot \mathbf{a}}{c_s^2} \left(1 + \frac{\boldsymbol{\xi}_\alpha \cdot \mathbf{u}}{c_s^2} \right) - \frac{\mathbf{a} \cdot \mathbf{u}}{c_s^2} \right\}, \quad (6)$$

where \mathbf{a} is an acceleration rate.

The presently applied scheme of the D3Q27 MRT-LBM was validated by conducting DNS of the turbulent channel flow in Kim et al. (1987) at $\text{Re}_\tau = 180$. The turbulence statistics, including the higher order turbulence correlations such as the budget terms in the turbulence energy equation and the predicted energy spectra, showed almost perfect agreement with those obtained using the spectrum method. Thus, the accuracy of this D3Q27 MRT-LBM was found to be equivalent to that of the spectral method (see, Suga et al. (2015)).

3. Macroscopic modeling of flows within rough walls

Spatial averaging is applied to the governing equations in order to macroscopically treat a flow inside a rough wall. In order to take account of rough wall characteristics which vary drastically depending on the rough

wall-normal coordinate, a representative elementary plane (REP) is considered parallel to the rough wall, as shown in Fig.1. Introducing the REP allows us to describe local averaged flow variables over the REP. A similar idea was introduced into the volume-averaged Navier-Stokes (VANS) model for porous medium flows or canopy flows Dwyer et al. (1997); Watanabe (2004); Breugem et al. (2006). The definition of the superficial plane-averaging of ϕ is introduced as follows:

$$\langle \phi \rangle = \frac{1}{A_S} \int_S \phi dS, \quad (7)$$

where S and A_S are the REP for spatial averaging and the plane area of S , respectively. A variable ϕ can be decomposed into contributions from an intrinsic (fluid phase) averaged value ($\langle \phi \rangle^f$) and a deviation from the intrinsic averaged value ($\tilde{\phi}$) as follows:

$$\phi = \langle \phi \rangle^f + \tilde{\phi}, \quad (8)$$

where the following relationship exists between the superficial and intrinsic plane-averaged values: $\langle \phi \rangle = \varphi \langle \phi \rangle^f$. Here, the plane porosity φ is defined as $\varphi = A_{S_f}/A_S$, where A_{S_f} denotes plane area of the fluid phase contained within the REP. Following Whitaker (1986), the plane-averaged continuity and momentum equations for incompressible flows can be respectively derived as

$$\frac{1}{\varphi} \frac{\partial \varphi \langle u_i \rangle^f}{\partial x_i} = 0 \quad (9)$$

$$\begin{aligned}
\frac{\partial \langle u_i \rangle^f}{\partial t} + \langle u_i \rangle^f \frac{\partial \langle u_j \rangle^f}{\partial x_j} &= -\frac{1}{\rho} \frac{\partial \langle p \rangle^f}{\partial x_i} + \frac{1}{\varphi} \frac{\partial}{\partial x_j} \left(\nu \frac{\partial \varphi \langle u_i \rangle^f}{\partial x_j} \right) \\
&\quad - \frac{1}{\varphi} \frac{\partial}{\partial x_j} \underbrace{\varphi \langle \tilde{u}_i \tilde{u}_j \rangle^f}_{\tau_{ij}} - \underbrace{\frac{\nu}{\varphi} \frac{\partial \varphi}{\partial x_j} \frac{\partial \langle u_i \rangle^f}{\partial x_j}}_{g_i^\varphi} \\
&\quad - \underbrace{\left(\frac{1}{\rho A_{S_f}} \int_L \tilde{p} n_i d\ell - \frac{\nu}{A_{S_f}} \int_L n_k \frac{\partial \tilde{u}_i}{\partial x_k} d\ell \right)}_{f_i}, \quad (10)
\end{aligned}$$

where L is the obstacle perimeter within the REP, ℓ is the circumference length of solid obstacles, and n_k is its unit normal vector pointing outward from the fluid to the solid phase. A stress term τ_{ij} consisting of velocity dispersion $\tilde{\mathbf{u}}$ is a subfilter-scale stress, and an inhomogeneous correction term g_i^φ appears due to inhomogeneity of the plane porosity φ . The term f_i is the plane-averaged drag force, which is expressed as a line integral of the dispersive viscous stress and the dispersive pressure. The unknown terms τ_{ij} and f_i must be modeled in order to solve the plane-averaged equation. The contribution of velocity dispersion to momentum transfer near the randomly distributed semi-sphere roughness was investigated by Kuwata and Kawaguchi (2018), and they concluded that the dispersive shear stress generated by the mean velocity dispersion contribution was smaller compared with the other stress terms, namely, the Reynolds shear stress, viscous stress, and drag force contribution terms. Indeed, they reported that the contribution of the dispersive shear stress to the skin friction coefficient was 3% at most. Another report on the dispersive shear stress profiles over a rough graphite surface was provided by Busse et al. (2015), and their results also confirmed the small contribution of the dispersive shear stress compared with the other stress terms. In addition, verification of dropping τ_{ij} for turbulence

over cube roughness was also confirmed by Breugem and Boersma (2005); Kuwata and Suga (2016c). Therefore, this study only models the plane-averaged drag force (verification of dropping τ_{ij} is discussed in §5.4). Since the plane-averaged drag force term should vanish outside rough walls, the transitional behavior of f_i near the rough wall/clear fluid interface region needs modeling. To model such behavior, Busse and Sandham (2012) introduced the shape function which regulated an influence of f_i with respect to a distance from the wall. Another approach is assuming a porosity profile near the interface region (Breugem et al., 2006; Kuwata and Suga, 2013; Kuwata et al., 2014; Kuwata and Suga, 2015c). However, rigorous validity of those treatments has yet to be confirmed. In this approach, in order to roughly model the transitional behavior of f_i , we consider flows through sparsely distributed random semi-spheres as illustrated in Fig.1. In such circumstances, the mutual dependence among the drag force acting on each roughness element is negligibly small. Therefore, the plane-averaged drag force term f_i can be assumed to be the arithmetic spatial averaged force acting on the two-dimensional solid circle of diameter $D(n)$ in the REP:

$$\rho f_i \approx \frac{1}{A_{S_f}} \sum_{n=1}^N D(n) C_D(n) \frac{\rho}{2} \langle \hat{u}_i \rangle^f \sqrt{\langle \hat{u}_k \rangle^f \langle \hat{u}_k \rangle^f}, \quad (11)$$

where N is the total number of the circles appearing in the REP, \hat{u} is the relative velocity to the rough surface ($\hat{u} = u - u_{rough}$). Here, u_{rough} is the moving velocity of the rough surface. Considering viscous and inertial effects, the drag coefficient $C_D(n)$ can be modeled as follows:

$$C_D(n) = \frac{C_1}{Re_D(n)} + C_2, \quad (12)$$

where C_1 and C_2 are the model constants that depend on the shape of the obstacle. The Reynolds number based on the circle diameter $Re_D(n)$ is defined as follows:

$$Re_D(n) = D(n) \sqrt{\langle \hat{u}_k \rangle^f \langle \hat{u}_k \rangle^f} / \nu. \quad (13)$$

Substituting Eqs. (8) and (13) into Eq. (11), the plane-averaged drag force can be written as

$$f_i = \nu \frac{C_1}{2} \frac{N}{A_{S_f}} \langle \hat{u}_i \rangle^f + \frac{C_2}{2} \langle \hat{u}_i \rangle^f \sqrt{\langle \hat{u}_k \rangle^f \langle \hat{u}_k \rangle^f} \frac{1}{A_{S_f}} \sum_{n=1}^N D(n). \quad (14)$$

Since generic (not idealized) rough surfaces cannot always be assumed to be the random semi-sphere cluster shown in Fig.1, prescribing a total number of circles N and the circle diameter $D(n)$ for generic rough surfaces is not straightforward, thus an alternative parameter for $D(n)$ is required. Hence, the present model introduces the plane hydraulic (equivalent) diameter D_m , defined as

$$D_m = \frac{4S_{sum}}{L_{sum}}, \quad (15)$$

where S_{sum} and L_{sum} are the total area occupied by the obstacles and the total wetted perimeter of the obstacles in the REP, respectively. They are written as

$$\begin{aligned} D_m = \frac{4S_{sum}}{L_{sum}} &= 4 \left(\sum_{n=1}^N \frac{\pi D(n)^2}{4} \right) / \left(\sum_{n=1}^N \pi D(n) \right) \\ &= 4(A_S - A_{S_f}) / \left(\sum_{n=1}^N \pi D(n) \right). \end{aligned} \quad (16)$$

Assuming that the total area occupied by the obstacles $A_S - A_{S_f}$ can be approximated as a product of the total number of circles N and the mean

circle area is $\frac{\pi}{4}D_m^2$, we have

$$A_S - A_{S_f} = N \times \left(\frac{\pi}{4} D_m^2 \right), \quad (17)$$

With the help of Eqs.(17) and (16), the plane-averaged drag force of Eq.(14) is further written as

$$f_i = \nu C_1^D \langle \hat{u}_i \rangle^f + C_2^D \langle \hat{u}_i \rangle^f \sqrt{\langle \hat{u}_k \rangle^f \langle \hat{u}_k \rangle^f}, \quad (18)$$

where the drag model coefficients for the linear and quadratic terms with respect to the plane-averaged velocity are expressed in terms of the plane porosity and plane hydraulic diameter as follows:

$$C_1^D = \frac{2C_1}{\pi} \frac{(1-\varphi)}{\varphi D_m^2}, \quad C_2^D = \frac{2C_2}{\pi} \frac{(1-\varphi)}{\varphi D_m}. \quad (19)$$

One should note that those model coefficients are only valid in the rough wall/clear fluid interface region where the distribution of roughness elements is sparse enough to neglect the mutual dependence among roughness elements. To correct the behavior of f_i in densely distributed roughness elements ($\varphi \approx 0$), correction functions f_1^d and f_2^d are introduced as follows:

$$C_1^D = \frac{2C_1}{\pi} \frac{(1-\varphi)}{\varphi D_m^2} f_1^d, \quad C_2^D = \frac{2C_2}{\pi} \frac{(1-\varphi)}{\varphi D_m} f_2^d, \quad (20)$$

where the model constants $C_1 = 71$ and $C_2 = 0.79$ are presently used, and the correction functions are $f_1^d = 1/\varphi$ and $f_2^d = 1/\varphi^{1.5}$. All of these can be determined by fitting the model coefficients C_1^D and C_2^D to the DNS results (the model drag coefficients are discussed in §5.2). Although introduction of the correction functions of f_1^d and f_2^d seems to be rather ad hoc, it should be mentioned that the effects of those functions on turbulence over rough

walls is insignificant since the effect of f_1^d and f_2^d becomes significant only deep inside rough walls where fluid flows are nearly damped out. One should also take caution because rough wall structures are usually anisotropic; the model coefficients should vary depending on axial direction and should be expressed in tensorial form. However, it was reported by Busse and Sandham (2012) that the effect of the streamwise drag force on turbulence was the most significant, and the effects of the other components were far weaker. Therefore, the present model does not account for anisotropy in the drag coefficients, but rather concentrates on modeling the in-plane components of the drag force.

Since we assume the drag coefficient to be a function of the Reynolds number as shown in Eq.(8), the present drag force model consists of two contributing terms, namely, viscous drag (a linear term) and foam drag (a quadratic term). This modeled form is the same as that of the modified Ergun equation (Macdonald et al., 1979), which is the drag force model for flows in porous media. Macdonald et al. (1979) confirmed that the modified Ergun equation could reasonably capture the Reynolds number dependence of the drag for several types of porous materials using a large amount of experimental data for porous medium flows. However, they also stated that suitable values of the model parameters in the modified Ergun equation were dependent on the structure of the porous medium. From these observations, one would expect that the present model also has the potential to reproduce the Reynolds number dependence. However, the presently proposed model constants and functions (C_1 , C_2 , f_1^d , and f_2^d) may require modification when one attempts to apply the model to the other types of rough surfaces. Further

investigation for different types of rough surfaces will be required to extend the applicability of the developed model.

4. Flow geometry and computational setup

In order to evaluate the developed macroscopic rough wall model, we performed DNS of open channel flows over irregularly distributed semi-spheres, as shown in Figure 2. Aside from simulations over the macroscopic rough wall that solves the plane-averaged Navier-Stokes equations in the rough wall region, DNS of fully resolved roughness is also carried out for rigorous model evaluation. To discuss the difference of the rough wall treatment, turbulent flow simulations over resolved and modeled rough walls are performed under the same numerical conditions, except for the rough wall. Periodic boundary conditions are applied to the streamwise and spanwise boundary faces, and a slip boundary is considered for the top boundary face. The resolved wall DNS imposes a non-slip boundary condition on the rough surfaces through a linear interpolated bounce-back scheme, while the macroscopic model simulation solves the plane-averaged momentum equation with the plane-averaged drag force model defined in Eq.(18). The details of the numerical method for the macroscopic model is described in Appendix A. For the bottom wall in the model simulation, the non-slip boundary condition is imposed by applying the half-way bounce-back method. The computational domain size of $L_x \times L_y \times L_z$ is set to $6\delta(x) \times \delta(y) \times 3\delta(z)$. The Reynolds number based on the averaged friction velocity at the rough wall u_τ and δ is set to 300. The computational domain is decomposed into finer and coarser resolution domains using the imbalance-correction zonal grid refinement method (Kuwata

and Suga, 2016a). The twice-finer uniform grid (equilateral cube grid) block is allocated near the rough wall region ($y/\delta \leq 0.35$), while the coarser uniform grid block is set away from the rough wall ($0.35 < y/\delta$). The number of grid nodes in the finer and coarser domains are $1201(x) \times 70(y) \times 601(z)$ and $601(x) \times 66(y) \times 301(z)$, respectively. The resolution in the finer and coarser grid regions are approximately 1.5 and 3.0 wall units, respectively. This grid resolution is comparable to those used in other lattice Boltzmann DNS studies (Lammers et al., 2006; Kuwata and Suga, 2016b,c; Gehrke et al., 2017). Moreover, to ensure validity of the simulation results, grid independence is carefully checked by comparing the turbulent intensities with those obtained using a factor 1.5 finer mesh simulation along each direction. The computational domain size is also confirmed to be sufficient by comparing the simulation results with those obtained from a box simulation that was a factor 2 larger.

The average friction velocity at the rough wall u_τ is given by the balance between the pressure drop ΔP and the averaged wall shear stress of the rough wall $\tau_w = \rho u_\tau^2$ as follows:

$$S_{in}\Delta P = L_x L_z \tau_w, \quad (21)$$

where S_{in} is the inlet boundary face area of fluid phase, which can be written as $S_{in} \approx L_z \delta_{eff}$. Here, the effective boundary layer thickness is defined as $\delta_{eff} = \int_0^\delta \varphi dy$. Thus, u_τ is

$$u_\tau = \left(\frac{\Delta P}{\rho} \frac{\delta_{eff}}{L_x} \right)^{0.5}. \quad (22)$$

The flow is driven by imposing a pressure difference in the streamwise direction. Note that since the effective boundary layer thickness δ_{eff} depends

on the plane porosity profiles, the streamwise pressure difference for all cases are different, even though the friction velocity is fixed.

Solving the plane-averaged momentum equation using the LBM requires including additional terms, e.g., the external force term in the lattice Boltzmann equation (Eq.(6)). Note that the relative velocity $\hat{\mathbf{u}}$ in Eq.(11) is the same as the fluid velocity $\langle \mathbf{u} \rangle^f$ because the present roughness is stationary.

The rough walls we considered consist of irregularly packed semi-spheres, as shown in Figure 2. The semi-sphere diameters follow a Gaussian distribution, and the semi-spheres are irregularly packed at a solid wall. The key roughness parameters in the developed drag force model are the plane porosity and the plane hydraulic diameter. Hence, to systematically discuss the influence of those parameters, the plane porosity and plane hydraulic diameter are designed to significantly vary just below the roughness peak. The mean diameter is $\mu/\delta = 0.2$, while the standard deviation of the Gaussian distribution is varied in three cases: $\sigma/\mu = 0.0, 0.17, 0.33$. The total number of semi-spheres is chosen so that the generated rough surface samples have nearly the same roughness parameters at the bottom wall.

Rough surfaces are generated with different roughness values and are denoted case I, II, and III. The probability density function of the rough surface height $h(x, z)$ is shown in Figure 3. Characteristics parameters for the rough wall, such as the number of semi-spheres N_s , maximum peak height of the roughness elements h_{max} , and statistical moments of the surface height

profiles, are defined as:

$$h_m = \frac{1}{L_x L_z} \int \int h(x, z) dx dz, \quad (23)$$

$$h_{rms} = \left(\frac{1}{L_x L_z} \int \int (h(x, z) - h_m)^2 dx dz \right)^{1/2}, \quad (24)$$

$$Sk = \left(\frac{1}{L_x L_z} \int \int (h(x, z) - h_m)^3 dx dz \right) / h_{rms}^3, \quad (25)$$

all of which are listed in Table 4. Here, h_m , h_{rms} , and Sk represent the mean height, standard deviation, and skewness of the roughness elevation, respectively. It is found from Fig.3 that roughness elements of $h^+(x, z) \approx 25$ primarily occupy the rough wall in case I, whereas higher and sparser roughness elements increasingly exist in cases II and III. The presence of the higher and sparser roughness elements is characterized by the large h_{rms}^+ and positive Sk values, as listed in Table 4, whereas the substantial negative value of Sk in case I indicates the presence of intermittently distributed deep valleys.

Before performing our simulations, we discuss an adequate physical size of the REP that is required to compute the roughness parameters (i.e., the plane porosity φ and plane hydraulic diameter D_m), both of which are required in the present macroscopic model. We consider the REP to be an orthogonal plane to the wall-normal coordinate. The topological parameters φ and D_m are expressed as a function of the wall-normal coordinate, whereas the instantaneous flow variables obtained from Eqs. (9) and (10) vary depending on not only the wall-normal coordinate but also the streamwise and spanwise coordinates. When we select the sufficiently large REP such that the averaged roughness parameters are independent of the size of the selected plane, the topological parameters φ and D_m are simply expressed as a func-

tion of the wall-normal coordinate, whereas the instantaneous flow variables obtained from Eqs. (9) and (10) vary depending on not only the wall-normal coordinate but also the streamwise and spanwise coordinates. Moreover, the advantage of the choice of the sufficiently large REP is that we do not have to consider the additional source terms related to the streamwise and spanwise gradient of φ in the governing equations, and it is therefore computationally efficient. By contrast, it is noted that choice of smaller REP is effective when we apply the developed model to the streamwise or spanwise heterogeneous rough surfaces whose roughness density significantly varied in streamwise or spanwise directions (e.g., Anderson et al., 2015). Figure 4 shows the convergence of the roughness parameters by increasing the size of the REP from $\frac{1}{8}L_x(x) \times \frac{1}{8}L_z(z)$ to $L_x(x) \times L_z(z)$. Fig.4(a) shows that the plane porosity profiles in case I nearly overlap except for the result with an REP size of $\frac{1}{8}L_x(x) \times \frac{1}{8}L_z(z)$. In Fig.4(b), D_m exhibits a substantial dependence of the REP near the bottom wall in case I, while D_m becomes large due to merged semi-spheres. This occurs because the larger REP is essentially required to correctly compute the larger hydraulic diameter. In this region, convergence of D_m within 10% can be confirmed when the size of the REP is larger than $\frac{1}{2}L_x(x) \times \frac{1}{2}L_z(z)$, which includes approximately 400 semi-spheres. In case III, one can see from Fig.4 (c) and (d) that the dependence of the REP size on the roughness parameters is more prominent. The relative difference in φ is less than 10% when we set the size of the REP to be larger than $\frac{1}{2}L_x(x) \times \frac{1}{2}L_z(z)$, which includes approximately 360 semi-spheres. Convergence within 10% is also confirmed with respect to D_m near the bottom wall region ($0.0 < y/\delta < 0.15$). However, the relative difference in D_m is signif-

icant as it departs from the bottom wall where the roughness elements are sparsely distributed. Although we can determine the arbitrary size of the REP, the present study determines the size of the REP as $L_x(x) \times L_z(z)$ and simply treats the roughness parameters as a function of the wall-normal coordinate only (see Appendix B for the discussion on the influence of the REP size on the simulation results).

Figure 5 show the plane porosity φ and plane hydraulic diameter D_m profiles when the REP size is set to $L_x(x) \times L_z(z)$. Since the roughness elements vanish outside the rough wall region, φ and D_m converge to unity and zero, respectively, outside the bottom rough wall. On the other hand, φ decreases and D_m increase in the vicinity of the bottom of the rough wall at $y/\delta = 0$. As the wall-roughness increases from case I to III, the convergence of φ to unity slows, as shown in Fig.5(a), and the region where D_m plateaus ($0.1 < y/\delta < 0.15$ in case II and $0.1 < y/\delta < 0.2$ in case III) extends, as shown in Fig.5(b). These results indicate a moderate change in the model coefficients for the plane-averaged drag force model. Furthermore, the plane hydraulic diameter D_m in case III is found to show a peak below the maximum rough wall height at $y/\delta \sim 0.22$, which is due the presence of the larger and sparser roughness elements quantified by positive Sk , as listed in Table 4.

5. Results and Discussions

5.1. Mean velocity and Reynolds stress

To discuss effects of the macroscopically modeled rough wall on standard turbulence statistics, we compared the streamwise mean velocity and

Reynolds stress profiles between the DNS and model simulation results. Figure 6 shows the profiles of the superficial plane-averaged streamwise mean velocity $U^+ = \varphi \langle \bar{u}^+ \rangle^f$. The DNS result in the smooth wall case is also plotted for comparison. As the wall-roughness increases, the damping effect in the streamwise mean velocity due to the rough surface is more pronounced, and the streamwise mean velocity at the top slip boundary ($y/\delta = 1.0$) shows a lower value compared with the smooth wall case, which is due to the increased skin friction coefficient on the rough wall. The downward shift of U^+ , which is referred to as the roughness function ΔU^+ , the skin friction coefficient $C_f = \tau_w / (0.5 \rho U_b^2)$, and the bulk mean Reynolds number $Re_b = U_b(2\delta)/\nu$ are listed in Table 5. One can see that the significant increase in ΔU^+ and C_f in the DNS results is quantitatively captured by the present model. Corresponding to the increase in ΔU^+ and C_f , the bulk mean Reynolds number decreases. The difference in C_f between the DNS and model simulation results is 7.6% (case I) at most. This shows that the increased rough wall skin friction coefficient is successfully reproduced in the developed model. The present DNS results suggest that the influence of the wall-roughness (quantified by ΔU^+) increases as h_{rms}^+ and Sk increase. This finding agrees with the experimental observations reported in the literature (Flack and Schultz, 2010), where the equivalent roughness was increased as h_{rms}^+ and Sk increased.

Figure 7 compares the superficial plane-averaged Reynolds stresses $R_{ij}^{A+} = \varphi \langle \overline{u'_i u'_j} \rangle^{f+}$ near the rough wall region. Note that R_{ij}^A can be decomposed into the macro-scale Reynolds stress R_{ij} and the micro-scale (subfilter-scale)

Reynolds stress r_{ij} as follows:

$$R_{ij}^A = \varphi \overline{\langle u'_i u'_j \rangle}^f = \underbrace{\overline{\langle u'_i \rangle^f \langle u'_j \rangle^f}}_{R_{ij}} + \underbrace{\varphi \overline{\langle \tilde{u}'_i \tilde{u}'_j \rangle}}_{r_{ij}}. \quad (26)$$

Since the DNS resolves the full details of turbulence near the roughness elements, the plane-averaged Reynolds stress in the present DNS includes r_{ij} and R_{ij} . On the other hand, the developed model macroscopically treats flows inside rough walls while neglecting the influence of velocity dispersion $\hat{\mathbf{u}}$. Thus, R_{ij}^A predicted by the present model does not include the contribution from r_{ij} . In Fig.7, as the wall-roughness increases from case I to III, the damping effect in R_{ij}^A due to roughness becomes more significant. In particular, the damping effect in the streamwise component in Fig.7(a) is more pronounced than in the other components in Fig.7(b) and (c), which is consistent with other experimental and DNS results (Ligrani and Moffat, 1986; Krogstad et al., 2005; Flack et al., 2007; Kuwata and Suga, 2016b,c). As the wall-roughness increases, the location of the maximum peak of R_{11}^A in Fig.7(a) moves away from the bottom wall, and the maximum peak value decreases. In contrast to the streamwise component, the wall-normal component in Fig.7(b) is found to be less sensitive to differences in the wall-roughness. Although the model simulation slightly underpredicts R_{22}^A and R_{33}^A inside the rough wall in case III, the overall agreement with the fully resolved DNS results is satisfactory, despite the fact that the model simulation ignores the contribution from r_{ij} . This may suggest that even though dispersion-related (micro-scale) turbulence may be slightly produced inside the rough walls, its contribution is far smaller than the that due to the macro-scale velocity fluctuations in the presently-tested rough walls.

5.2. Plane-averaged drag force

In order to validate the plane-averaged drag force model, Figure 8 compares the model coefficients for the linear (first) and quadratic (second) drag force terms C_1^D and C_2^D . The lines indicate the profiles modeled with Eq.(20), while the symbols are obtained by directly computing the plane-averaged drag force with Eq.(10) from the DNS results. The DNS simulations are performed at two Reynolds numbers in order to obtain the two model coefficients. Low Reynolds number laminar flow simulations are conducted to obtain the model coefficient in the linear term C_1^D , which predominantly works in the low Reynolds number regime. That in the quadratic term C_2^D is obtained from the turbulent flow simulation, where the linear and quadratic terms work. Fig.8 shows that both C_1^D and C_2^D drastically increase toward the bottom solid wall (at $y/\delta = 0$) because flows are completely damped at the bottom wall. Even though C_1^D in case III exhibits very complicated behavior, one can see that the present model for C_1^D can perfectly capture the trend of the DNS results. Although the trends of C_1^D and C_2^D are roughly similar, differences can be seen near the interface region ($y/\delta \approx 0.25$) in case III. The profile of C_1^D in case III shows plateau near the interface region, whereas C_2^D monotonically decreases as approaching to the maximum rough wall height at $y = h_{max}$. Although the developed model over-predicts C_2^D in this region, as shown in Fig.8(b), the overall agreement with the DNS data is confirmed. This emphasizes that the plane porosity and the plane hydraulic diameter are considerably effective parameters for modeling the plane-averaged drag force.

5.3. Turbulence structures

It is well-known that turbulence structures over a rough wall are very different from that over a smooth wall. Accordingly, the turbulence structures over the modeled and resolved walls are compared in order to assess whether the macroscopic model can reproduce turbulence.

Figure 9 shows snapshots of the instantaneous wall-normal vorticity fluctuations at the position of the maximum roughness height ($y = h_{max}$). The DNS and model simulation results show high and low speed streaks develop over the rough wall of case I, which we usually observe in the vicinity of a smooth wall, whereas streaky structures in cases II and III are less organized and lose their strength. Although the turbulence structures over the modeled rough walls of cases I and II (Fig.9(a) and (b), respectively) are very similar to those over the resolved rough walls, clear difference can be observed in case III, as shown in Fig.9(c). In case III shown in Fig.9(c), the streamwise elongated structure over the resolved rough wall is very shredded, while that over the modeled wall appears to be smoother and more interconnected.

To discuss the fluctuating vorticity intensity, Figure 10 compares the root mean square of the superficial plane-averaged vorticity fluctuation defined as $\omega = \varphi \langle \nabla \times \mathbf{u} \rangle^f$. The results confirm that these fluctuations lose strength as the wall-roughness increases (cases II and III), although the pointed peak of $\omega_{y,rms}^+$ can be seen at the maximum roughness height in case I. This fact substantiates the disappearing of the high-and low-speed streaks, as shown in Fig.9 (b) and (c). However, the reduction in the streamwise and spanwise components in cases II and III is less significant than that of the wall-normal component. The vorticity fluctuations in all components are rapidly damped

inside the rough wall for case I, whereas they increase and exhibit peak inside the rough walls for cases II and III. This implies that turbulent vortex motion inside the rough walls increases due to the roughness elements, although the development of streaky structures over the rough wall is prevented in cases II and III. The vorticity fluctuations predicted by the developed model in case I agree well with the DNS data, whereas the developed model significantly under-predicts vorticity fluctuations inside the rough wall for cases II and III. The possible explanation for this under-prediction is that the vorticity fluctuation related to velocity dispersion, which is neglected in the model simulation, is of significant inside the rough wall for cases II and III. The instantaneous vorticity $\boldsymbol{\omega} = \nabla \times \boldsymbol{u}$ inside the rough wall can be also decomposed into the macro-scale part $\nabla \times \langle \boldsymbol{u} \rangle^f$ and the micro-scale part (dispersion-related vorticity) $\nabla \times \tilde{\boldsymbol{u}}$. Inside the rough wall in cases II and III, turbulent eddies penetrate deep inside the rough wall, break into small-scale structures, and finally dissipate. Thus, it is expected that the contribution from the micro-scale (dispersion-related) vorticity is not negligibly small inside the rough wall for cases II and III. Indeed, due to the break down into small-scale turbulent vortex motion, the turbulence structure over the resolved rough wall is more shredded and disordered than that over the modeled wall, as shown in Fig.9(c).

5.4. Momentum transfer

In order to confirm the validity of the developed model in more detail, momentum transfer near the rough walls is examined by analyzing the plane and Reynolds (double) averaged momentum equations. Applying integration to the double averaged momentum equation over the wall-normal direction

from 0 to y , the integrated momentum equation can be written as

$$\begin{aligned} \int_0^y \frac{D\langle u \rangle^f}{Dt} dy &= -\frac{1}{\rho} \frac{\partial \langle \bar{p} \rangle^f}{\partial x} \int_0^y \varphi dy + \nu \underbrace{\frac{\partial \varphi \langle \bar{u} \rangle^f}{\partial y}}_{VS} \\ &\quad - \underbrace{\varphi \langle \tilde{u} \tilde{v} \rangle^f}_{DC} - \underbrace{\varphi \langle \overline{u'v'} \rangle^f}_{RS} \\ &\quad - \underbrace{\int_0^y \varphi \overline{g_x^\varphi} dy}_{IC} - \underbrace{\int_0^y \varphi \overline{f_x} dy}_{DF} = 0, \end{aligned} \quad (27)$$

Note that the plane-averaged viscous stress, plane-averaged Reynolds stress, and plane-dispersive covariance are assumed to be zero at the bottom wall. Since those stress terms also become zero at the top boundary, we can obtain the relationship by substituting $y = \delta$ into Eq. (27):

$$0 = -\frac{1}{\rho} \frac{\partial \langle \bar{p} \rangle^f}{\partial x} \int_0^\delta \varphi dy - \int_0^\delta \varphi \overline{g_x^\varphi} dy - \int_0^\delta \varphi \overline{f_x} dy. \quad (28)$$

After subtracting Eq.(28) from Eq.(27), the stress balance can be written as

$$\begin{aligned} 0 &= -\frac{1}{\rho} \frac{\partial \langle \bar{p} \rangle^f}{\partial x} \left(\int_0^\delta \varphi dy - \int_0^y \varphi dy \right) + \underbrace{\nu \frac{\partial \varphi \langle \bar{u} \rangle^f}{\partial y}}_{VS} \\ &\quad - \underbrace{\varphi \langle \tilde{u} \tilde{v} \rangle^f}_{DC} - \underbrace{\varphi \langle \overline{u'v'} \rangle^f}_{RS} - \underbrace{\left(\int_0^y \varphi \overline{g_x^\varphi} dy - \int_0^\delta \varphi \overline{g_x^\varphi} dy \right)}_{IC} \\ &\quad - \underbrace{\left(\int_0^y \varphi \overline{f_x} dy - \int_0^\delta \varphi \overline{f_x} dy \right)}_{DF}, \end{aligned} \quad (29)$$

where the terms VS, DC, RS, IC, and DF are the plane-averaged viscous stress, plane-dispersive covariance, plane-averaged Reynolds shear stress, inhomogeneous correction contribution, and plane-averaged drag force contribution terms, respectively. Figures 11 and 12 shows these terms normalized by u_τ . In Fig.11(a), the plane-averaged viscous stress (VS) exhibits a local maximum value at the maximum roughness height in case I, while the VS

profiles in cases II and III shown in Fig.11(b) and (c) exhibit peaks inside the rough walls. As the wall roughness increases, the damping effect on U^+ due to roughness is more relaxed, as shown in Fig.6. This reduces the mean velocity gradient, and the maximum peak value of VS decreases accordingly. The plane-averaged Reynolds shear stress (RS) becomes significant over the rough walls, while it rapidly decays to zero deep inside the rough walls for $y/\delta < 0.05$, where the Reynolds normal stress exists in this region as shown in Fig.7. This implies that the velocity fluctuations deep inside the rough walls exists but it hardly contributes to the increase in the Reynolds shear stress. The plane-dispersive covariant (DC) term is negligibly small in cases I and II. In contrast, DC is slightly generated near $y/\delta = 0.15$ for case III, and the maximum DC value reaches roughly half that of VS. The present model neglects DC, and a slight discrepancy can be observed in the RS profile for case III. However, a comparison between the model simulation and DNS results confirms almost perfect agreement of VS and RS for cases I and II.

Although VS, RS, and DC do not contribute to momentum transfer deep inside the rough walls, as shown in Fig.11, one finds in Fig.12 that the plane-averaged drag force contribution (DF) and inhomogeneous correction contribution (IC) terms predominantly work in this region. As the wall-roughness increases, the contribution of IC inside the rough wall decreases while the DF contribution increases. Corresponding to the moderate change of φ and D_m in case III, as shown in Fig.5, generation of DF is more moderate compared with those in cases I and II. The developed model over-predicts DF in case III due to the over-predicted model coefficient for the quadratic drag force

term C_2^D , as shown in Fig.8. However, this figure confirms that the present model reasonably captures the DF and IC trends.

5.5. Turbulence transport

In this subsection, we take a closer look at the turbulent transport mechanism near the resolved and modeled rough walls by analyzing the turbulence energy budget terms. The turbulence energy in DNS includes the contribution from velocity dispersion, whereas that for the model simulation does not. Therefore, the transport equations of the volume-averaged turbulence energy $k^A = R_{kk}^A/2 = (R_{kk} + r_{kk})/2$ and the macro-scale turbulence energy $k = R_{kk}/2$ are considered in the DNS and the model simulation, respectively.

After applying volume averaging to the transport equation of the turbulence energy, the following transport equation for k^A can be derived:

$$\begin{aligned}
\frac{Dk^A}{Dt} = & \underbrace{-\frac{\partial}{\partial x_k} \left(\frac{\varphi}{2} \overline{\langle u'_i u'_i u'_k \rangle^f} \right)}_{D_{kA}^t} - \underbrace{\frac{\partial}{\partial x_k} \left(\varphi \frac{\overline{\langle u'_k p' \rangle^f}}{\rho} \right)}_{D_{kA}^p} \\
& + \underbrace{\frac{\partial}{\partial x_k} \left\langle \varphi \nu \frac{\partial \frac{1}{2} \overline{u'_i u'_i}}{\partial x_k} \right\rangle^f}_{D_{kA}^\nu} - \underbrace{\frac{\partial}{\partial x_k} \varphi \overline{\langle \tilde{u}_k u'_i u'_i \rangle^f}}_{D_{kA}^\tau} \\
& - \underbrace{\varphi \left\langle \overline{u'_i u'_k} \frac{\partial \overline{u_i}}{\partial x_k} \right\rangle^f}_{P_{kA}} - \underbrace{\varphi \left\langle \nu \frac{\partial \overline{u'_i}}{\partial x_k} \frac{\partial \overline{u'_i}}{\partial x_k} \right\rangle^f}_{\varepsilon_{kA}}, \tag{30}
\end{aligned}$$

where D_{kA}^t , D_{kA}^p , D_{kA}^ν , D_{kA}^τ , P_{kA} , and ε_{kA} are the turbulent diffusion, pressure diffusion, viscous diffusion, dispersion transport, production, and dissipation terms for the volume-averaged turbulence energy, respectively. Although further correlation terms are produced when the decomposition $u_i = \langle u_i \rangle^f + \tilde{u}_i$

is applied (Kuwata and Suga, 2013, 2015c), this study does not focus on those correlations because those correlation terms make it difficult to compare the results with those in the model simulation.

The macro-scale turbulence energy transport equation is discussed for the model simulation. Multiplying Eq.(10) by $\langle u'_i \rangle^f$ and averaging over time yields the transport equation of k :

$$\begin{aligned}
\frac{Dk}{Dt} = & \underbrace{-\frac{\partial}{\partial x_k} \left(\frac{\varphi}{2} \overline{\langle u'_i \rangle^f \langle u'_i \rangle^f \langle u'_k \rangle^f} \right)}_{D_k^t} - \underbrace{\frac{\partial}{\partial x_k} \left(\varphi \frac{\overline{\langle u'_k \rangle^f \langle p' \rangle^f}}{\rho} \right)}_{D_k^p} \\
& + \underbrace{\frac{\partial}{\partial x_k} \left(\varphi \nu \frac{\partial}{\partial x_k} \left(\frac{\overline{\langle u'_i u'_i \rangle^f}}{2} \right) \right)}_{D_k^\nu} + \underbrace{\nu \overline{\langle u'_i u'_i \rangle^f} \frac{\partial^2 \varphi}{\partial x_k^2}}_{G_k^\varphi} - \underbrace{\varphi \overline{\langle u'_i \rangle^f \langle u'_k \rangle^f} \frac{\partial \overline{\langle u_i \rangle^f}}{\partial x_k}}_{P_k} \\
& - \underbrace{\varphi \nu \frac{\partial \overline{\langle u'_i \rangle^f}}{\partial x_k} \frac{\partial \overline{\langle u'_i \rangle^f}}{\partial x_k}}_{\varepsilon_k} - \underbrace{\varphi \overline{f'_i \langle u'_i \rangle^f}}_{F_k}, \tag{31}
\end{aligned}$$

where D_k^t , D_k^p , D_k^ν , G_k^φ , P_k , ε_k and F_k are the turbulent diffusion, pressure diffusion, viscous diffusion, inhomogeneous correction, production, dissipation, and plane-averaged drag force terms for the macro-scale turbulence energy, respectively. It should be stressed that the transport equation for k does not include terms related to velocity dispersion but it includes the drag force term F_k .

Figure 13 compares the turbulence energy production, dissipation and, dispersion transport terms non-dimensionalized by u_τ^4/ν . The dispersion transport $D_{k^A}^\mathcal{T}$ in the DNS is confirmed to be negligibly small in all cases, suggesting that the mean velocity dispersion hardly contributes to turbulence energy diffusion. The turbulence production P_k^A in the DNS reaches

its maximum over the rough wall for case I, while the maximum peak of P_k^A decreases inside the rough wall for cases II and III. Although a slight discrepancy can be seen between the production terms from the model simulation and DNS results inside the rough wall for case III, the overall agreement with the DNS data is very reasonable. However, in contrast to the production term, turbulence energy dissipation for the model simulation shows a significantly lower value than that for the DNS. Since ε_{k^A} can be decomposed into the energy dissipation for the macro-scale turbulence ε_k and the micro-scale (dispersion-related) turbulence ε_m :

$$\varepsilon_{k^A} = -\varphi \left\langle \nu \frac{\partial u'_i}{\partial x_k} \frac{\partial u'_i}{\partial x_k} \right\rangle^f = -\underbrace{\varphi \left\langle \nu \frac{\partial \tilde{u}'_i}{\partial x_k} \frac{\partial \tilde{u}'_i}{\partial x_k} \right\rangle^f}_{\varepsilon_m} - \underbrace{\varphi \nu \frac{\partial \langle u'_i \rangle^f}{\partial x_k} \frac{\partial \langle u'_i \rangle^f}{\partial x_k}}_{\varepsilon_k}, \quad (32)$$

the underestimated energy dissipation can be attributed to the deficiency of ε_m , which the developed model fails to reproduce. This suggests that the velocity dispersion does not significantly contribute to turbulence production but plays an important role in energy dissipation. Greater turbulence energy dissipation in the DNS results indicates that small-scale turbulent eddy motions are more active in the DNS than in the model simulation. This can partly explain the under-prediction of vorticity fluctuations in Figs.9 and 10. The smallest length scale of the resolved eddy related to turbulence dissipation (Kolmogorov scale, defined as $\eta = (\nu^3/\varepsilon_{max})^{1/4}$) in the DNS are $\eta^+ = 1.45$ (case I), 1.74 (case II), and 1.94 (case III), and the ratios $\eta_{model}^+/\eta_{DNS}^+$ are 1.14 (case I), 1.11 (case II), and 1.14 (case III). The value of $\eta_{model}^+/\eta_{DNS}^+ = 1.14$ in cases I and III indicates that the model simulation can be performed with a factor 1.14 coarser mesh in each direction compared with the DNS, which means that the developed model can save roughly 30% of the total num-

ber of grid nodes in three dimensions. It is worth noting that, in spite of the under-predicted turbulence energy dissipation, the sum of ε_k^+ and F_k^+ coincides with the energy dissipation from the DNS results. This suggests that F_k^+ in the model simulation can recover the deficiency of the unresolved micro-scale energy dissipation ε_m^+ ($\varepsilon_m^+ \simeq F_k^+$). In terms of the role of F_k in energy transport, Pinson et al. (2007); Kuwata et al. (2014); Kuwata and Suga (2016c) stated that F_k played an role of the energy transfer from the macro-scale turbulence to the micro-scale turbulence. The present finding of $F_k \approx \varepsilon_m$ implies that the energy transferred from the macro-scale turbulence is locally balanced with ε_m . In other words, the micro-scale turbulence reaches local equilibrium.

The pressure and turbulent diffusion terms and the viscous term (non-dimensionalized by u_τ^4/ν) are compared in Figure 14. Note that the sum of the inhomogeneous correction term $G_k^{\varphi+}$ and viscous diffusion $D_k^{\nu+}$ is plotted as the viscous term for the model simulation. The turbulent, pressure diffusion, and viscous terms change sign from negative to positive deep inside the rough walls. This observation indicates that those terms carry turbulence inside the rough walls. However, as the wall-roughness increases, those terms become progressively smaller. This means that turbulence tends to approach local equilibrium. The behavior of those terms is confirmed to be quantitatively captured by the present model. Despite the fact that D_{kA}^t

includes many correlations related to velocity dispersion

$$D_{k^A}^t = -\frac{\partial}{\partial x_k} \varphi \langle \overline{u'_k u'_i u'_i} \rangle^f = \underbrace{-\frac{\partial}{\partial x_k} \varphi \langle u'_k \rangle^f \langle u'_i \rangle^f \langle u'_i \rangle^f}_{D_k^t} - \frac{\partial}{\partial x_k} \varphi \langle u'_k \rangle^f \langle \tilde{u}'_i \tilde{u}'_i \rangle^f - \frac{\partial}{\partial x_k} 2\varphi \langle \tilde{u}'_k \tilde{u}'_i \rangle^f \langle u'_i \rangle^f - \frac{\partial}{\partial x_k} \varphi \langle \tilde{u}'_k \tilde{u}'_i \tilde{u}'_i \rangle^f, \quad (33)$$

D_k^{t+} and $D_{k^A}^{t+}$ agree well. Hence, it can be concluded that the fluctuating velocity dispersion hardly contributes to turbulence diffusion.

6. Concluding remarks

A macroscopic rough wall model was developed based on spatial (plane) averaging theory in order to predict rough wall turbulence without resolving complicated rough geometries. The plane-averaged drag force term, which arises in the plane-averaged Navier-Stokes equations, is modeled with a plane porosity and plane hydraulic diameter. In order to evaluate the developed model, direct numerical simulation and macroscopic model simulation for turbulence over irregularly distributed semi-spheres in the transitionally rough regime are conducted using the D3Q27 multiple-relaxation-time lattice Boltzmann method. Three rough walls with different roughness are chosen for model evaluation. The remarks summarizing the present study are:

(1) The results confirm that the drag coefficients in the plane-averaged drag force model can be successfully modeled using two characteristic rough wall parameters, namely, the plane porosity and plane hydraulic diameter.

(2) The developed model can reproduce the significant increase in skin friction at the rough wall, and agreement of the predicted mean velocity and Reynolds stress profiles with the fully resolved DNS data is satisfactory.

(3) Turbulence structures over the resolved and modeled walls are very similar when the roughness is relatively small, whereas the turbulent structure over the resolved wall is more shredded and disordered compared with that over the modeled wall as the wall roughness increases. This is due to dispersion-related small scale vortex motion that is enhanced by the roughness elements, which the developed model cannot account for.

(4) The contribution of the plane-averaged drag force term to momentum transfer increases as the wall roughness increases. The plane-dispersive covariance, which is dropped in the present macroscopic model, slightly contributes to momentum transfer over surfaces with large roughness.

(5) Velocity and pressure dispersion do not contribute to the production and diffusion processes, while velocity dispersion considerably contributes to turbulence energy dissipation. However, the plane-averaged drag force term in the model can successfully recover deficiencies in unresolved turbulence energy dissipation.

Appendix A: Implementation of the macroscopic model

For the macroscopic model simulation, the modeled plane-averaged equations being solved are rewritten as follows:

$$\frac{\partial \langle u_i \rangle^f}{\partial x_i} + \underbrace{\frac{\langle u_i \rangle^f}{\varphi} \frac{\partial \varphi}{\partial x_i}}_{S_c} = 0, \quad (\text{A1})$$

$$\begin{aligned}
\frac{\partial \langle u_i \rangle^f}{\partial t} + \langle u_i \rangle^f \frac{\partial \langle u_j \rangle^f}{\partial x_j} &= -\frac{1}{\rho} \frac{\partial \langle p \rangle^f}{\partial x_i} + \frac{\partial}{\partial x_j} \left(\nu \frac{\partial \langle u_i \rangle^f}{\partial x_j} \right) \\
&\quad + \underbrace{\frac{\nu}{\varphi} \frac{\partial^2 \varphi}{\partial x_j^2} \langle u_i \rangle^f + 2 \frac{\nu}{\varphi} \frac{\partial \varphi}{\partial x_j} \frac{\partial \langle u_i \rangle^f}{\partial x_j}}_{S_{m,i}} - g_i^\varphi - f_i,
\end{aligned} \tag{A2}$$

where S_c and $S_{m,i}$ are respectively the additional source term in the continuity and momentum equations, and the macroscopic rough wall model can be implemented by adding the source terms S_c and $S_{m,i}$ to the governing equations. Although the present study employs the lattice Boltzmann method for the model simulation, the proposed model can be applied with the other standard Navier–Stokes solvers such as a finite volume method and finite difference method. Moreover, for the Navier–Stokes solvers an introduction of the additional terms S_c and $S_{m,i}$ is much easier than resolving directly the rough geometry, and thus it can be said that the Navier–Stokes solvers takes more advantage of the macroscopic model compared with the lattice Boltzmann method. For the lattice Boltzmann method, the introduction of the mass source terms S_c is not straightforward. Hence, to remove the mass source term from the governing equation, the present study alternatively solves the superficial plane-averaged equations:

$$\frac{\partial \langle u_i \rangle}{\partial x_i} = 0, \tag{A3}$$

$$\begin{aligned}
\frac{\partial \langle u_i \rangle}{\partial t} + \langle u_i \rangle \frac{\partial \langle u_j \rangle}{\partial x_j} = & -\frac{1}{\rho} \frac{\partial \langle p \rangle}{\partial x_i} + \frac{\partial}{\partial x_j} \left(\nu \frac{\partial \langle u_i \rangle}{\partial x_j} \right) \\
& + \underbrace{\frac{\langle p \rangle}{\rho \varphi} \frac{\partial \varphi}{\partial x_i} - \frac{\partial}{\partial x_j} \left[\left(1 - \frac{1}{\varphi} \right) \langle u_i \rangle \langle u_j \rangle \right]}_{S'_{m,i}} - g_i^\varphi - f_i.
\end{aligned} \tag{A4}$$

The additional source term $S'_{m,i}$ is calculated with a central difference scheme and introduced to the lattice Boltzmann equation with the external force model of Eq.(6). It is cautioned that g_i^φ and f_i should be evaluated with the intrinsic plane-averaged velocity $\langle u_i \rangle^f$, which is computed as $\langle u_i \rangle^f = \langle u_i \rangle / \varphi$.

Appendix B: Size of the representative elementary plane

In order to examine the influence of the size of the REP on the simulation results, we compare the simulation results in case III with two different REP of $L_x(x) \times L_z(z)$ and $\frac{1}{8}L_x(x) \times \frac{1}{8}L_z(z)$. As mentioned in §4, when we choose the smaller size of the REP as $\frac{1}{8}L_x(x) \times \frac{1}{8}L_z(z)$, the roughness parameters D_m and φ vary not only in the wall-normal direction but also in the spanwise and streamwise directions as can be observed in Fig.B1. For the simulation with the smaller REP, flow conditions are the same as in §4 but only the profiles of the roughness parameters D_m and φ differ. Figures B2 and B3 compare the plane-averaged mean velocity and turbulent intensity profiles. We confirm in Fig.B2 that the predicted mean velocity profiles with the smaller REP marginally shifts downward, indicating a slight increase in the rough wall skin friction coefficient. In Fig.B3, the simulation with the larger REP slightly overpredicts the streamwise turbulence intensity around $y/\delta = 0.2$ relative to the resolved DNS data while underpredicts deep inside the rough wall for

$y/\delta < 0.1$, and moreover, the predicted wall-normal turbulence intensity is slightly smaller inside the rough wall. Interestingly, clear improvement is confirmed in the simulation results with the smaller REP.

Finally, Fig.B4 depicts a comparison of the plane-averaged Reynolds shear stress RS, plane-dispersive covariance DC, and plane-averaged drag force contribution DF terms with the resolved DNS data. Figure B4 (a) confirms that the prediction of the plane-averaged Reynolds shear stress is improved by the smaller REP, corresponding to the improvement of the streamwise and wall-normal turbulence intensities as show in Fig.B3. The plane-dispersive covariance is slightly generated due to the streamwise and spanwise inhomogeneity of the roughness parameters as observed in Fig.B1; however, the predicted values are found to be far smaller relative to the resolved DNS results. In Fig.B4 (b), it is found that the plane-averaged drag force is not improved even with the smaller REP. These results suggest that the use of the smaller REP can slightly improve the turbulent intensity although the prediction of the mean velocity dispersion is hardly improved even with the streamwise and spanwise varied roughness parameter, and the use of the smaller REP hardly affects the prediction of the drag force.

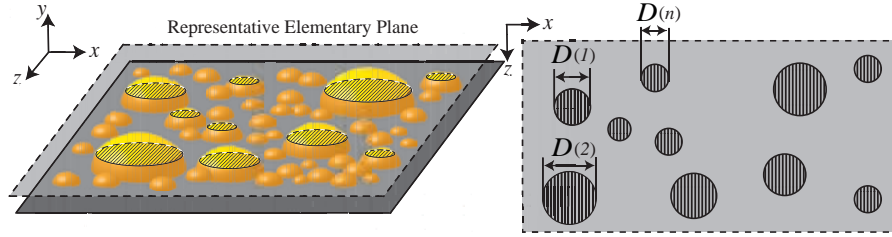


Figure 1: Sketch of the REP (representative elementary plane) for plane averaging.

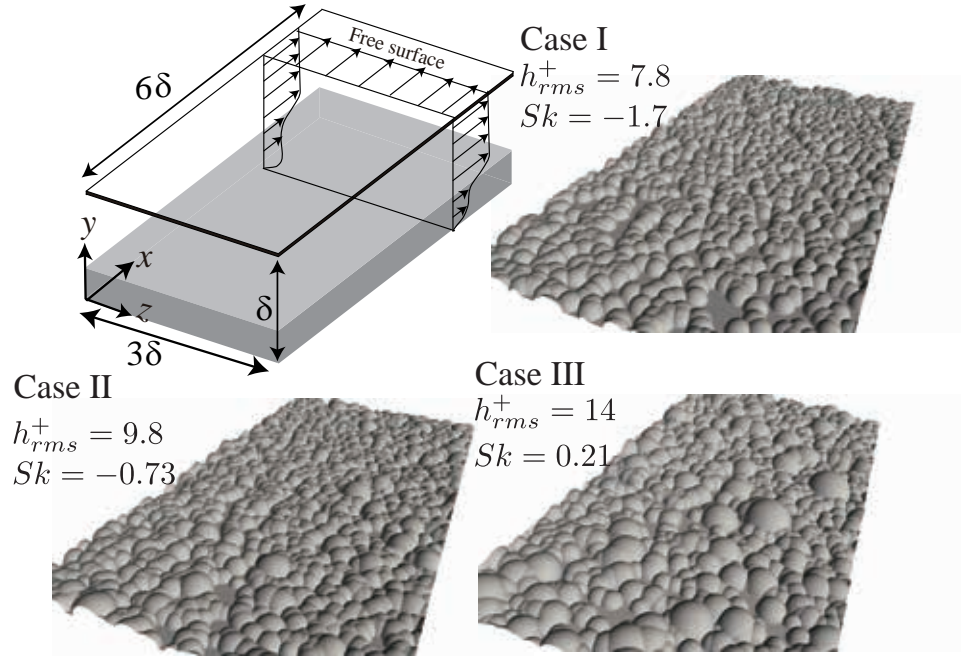


Figure 2: Computational geometry of rough-walled open channel flows.

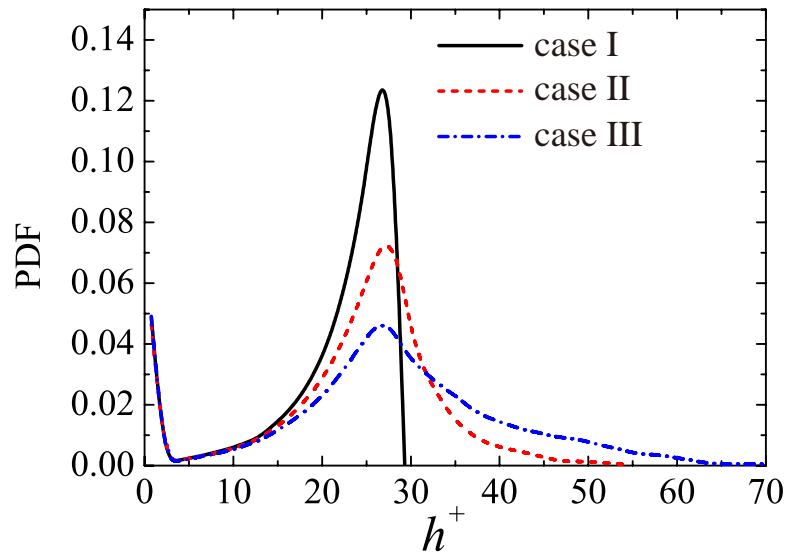


Figure 3: Probability density function of the rough surface height.

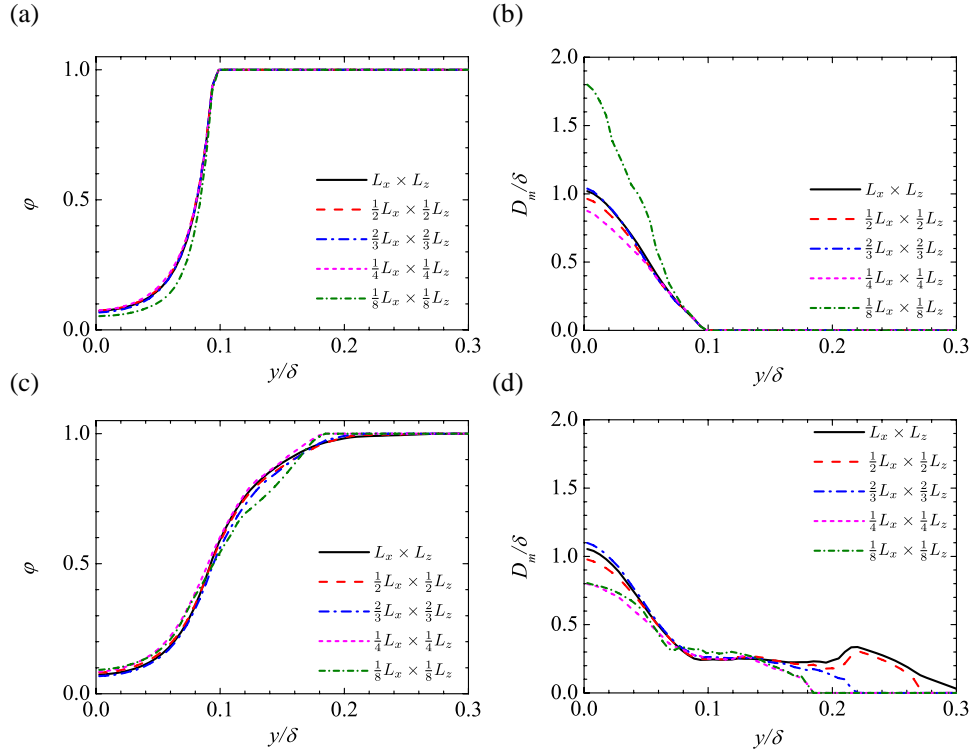


Figure 4: Influence of the size of REP on the roughness parameters: (a) φ in case I, (b) D_m in case I, (c) φ in case III, and (d) D_m in case III.

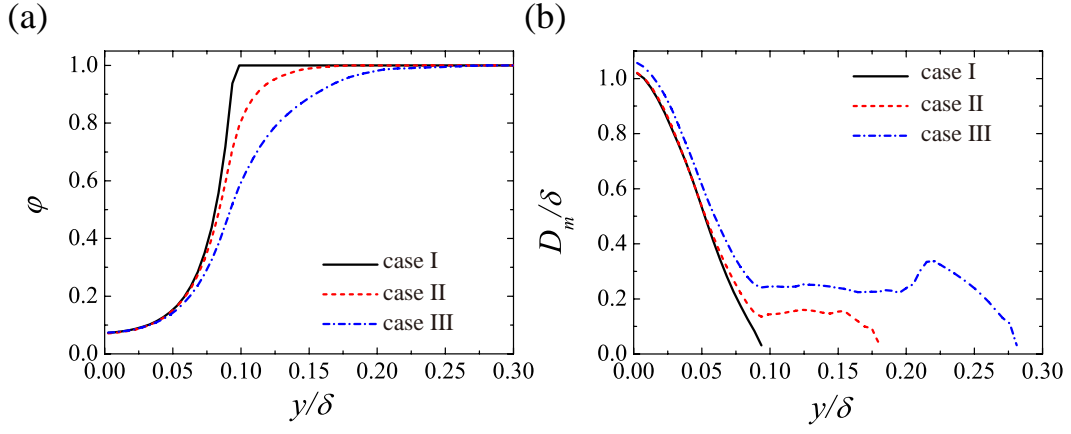


Figure 5: Characteristic parameters of the rough walls: (a) plane porosity ϕ and (b) plane hydraulic diameter D_m .

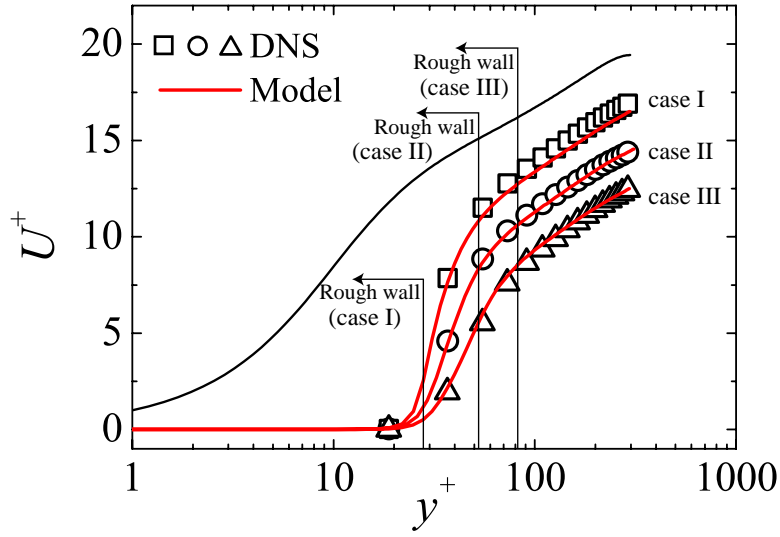


Figure 6: Comparison of the superficial plane-averaged streamwise mean velocity profiles.

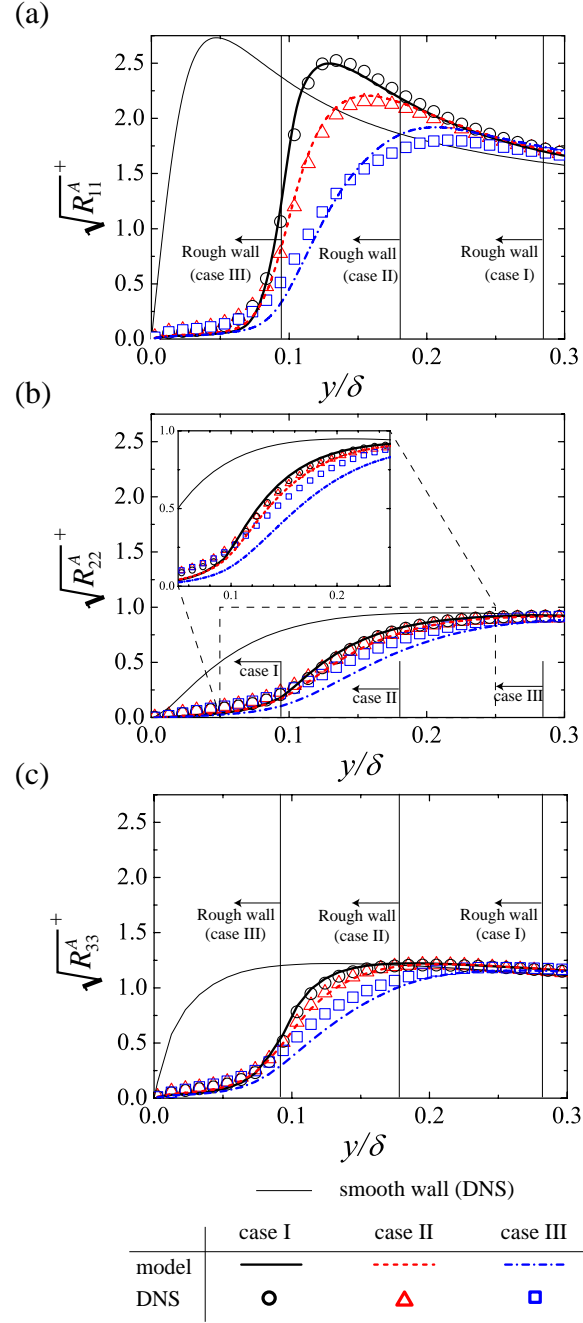


Figure 7: Comparison of the superficial plane-averaged Reynolds normal stresses: (a) streamwise, (b) wall-normal, and (c) spanwise components. The vertical solid line indicates the position of the roughness peak $y = h_{max}$.

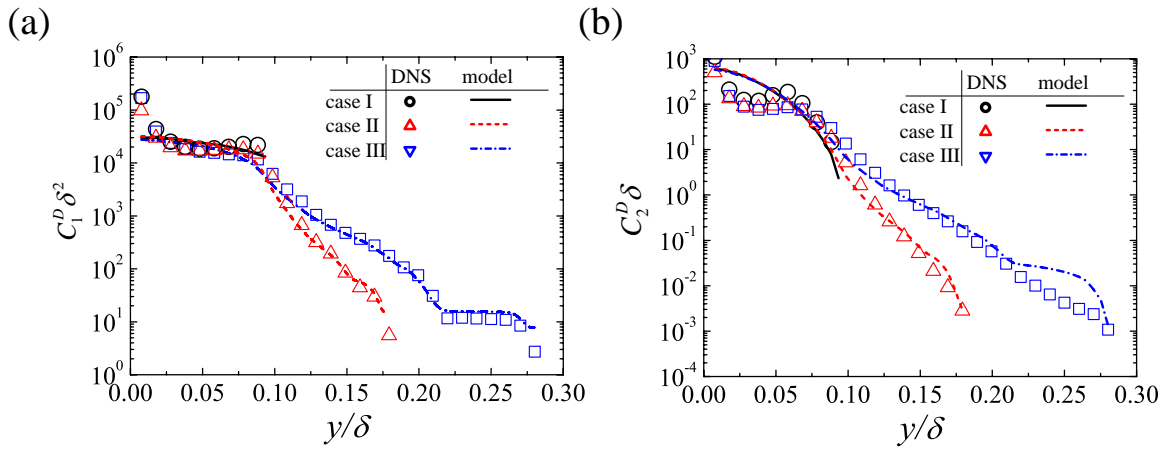
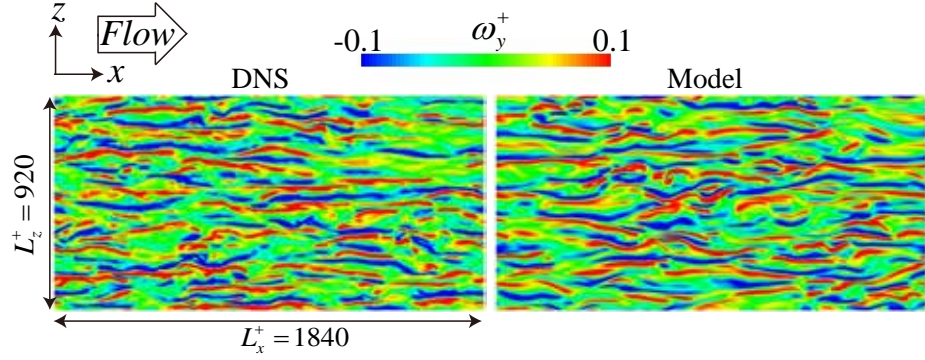
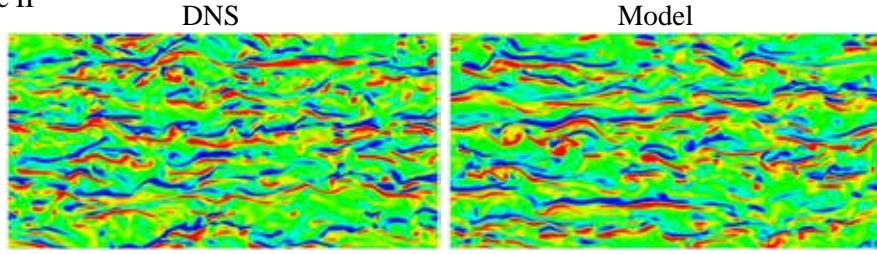


Figure 8: Comparison of the model coefficients for the plane-averaged drag force mode: (a) linear term coefficient and (b) quadratic term coefficient.

(a) case I



(b) case II



(c) case III

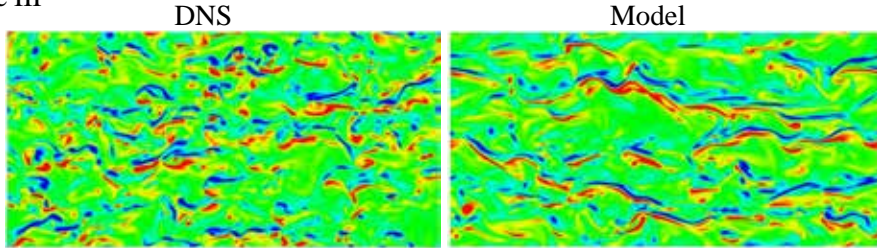


Figure 9: Comparison of instantaneous wall-normal vorticity fluctuations at the maximum rough wall height of $y = h_{max}$: (a) case I, (b) case II, and (c) case III.

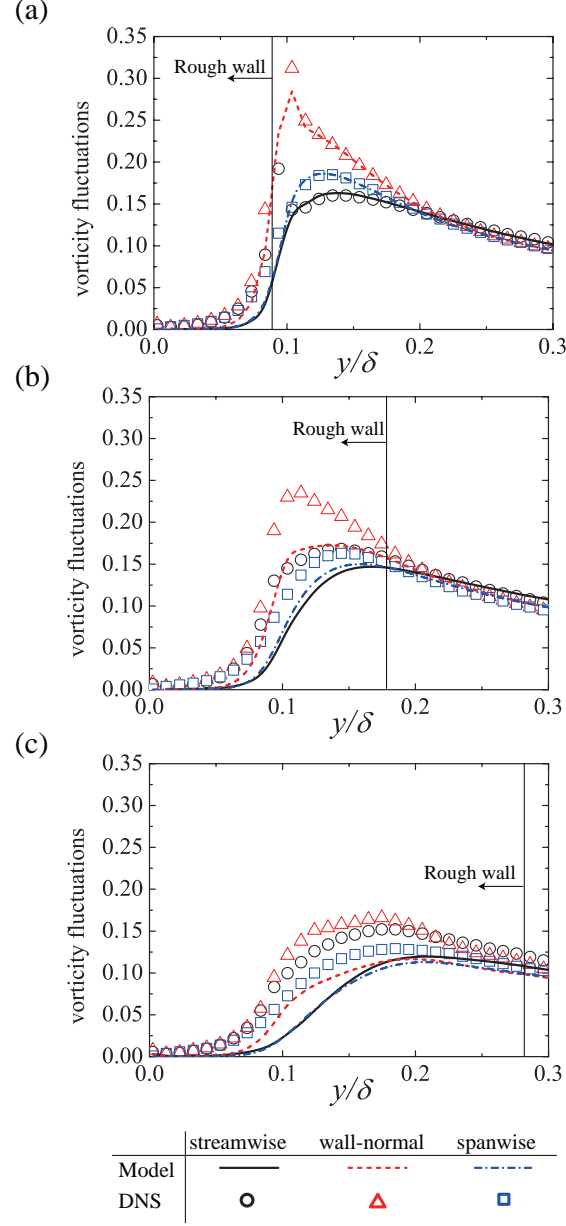


Figure 10: Comparison of the superficial plane-averaged vorticity intensities: (a) case I, (b) case II, and (c) case III. The vertical solid line indicates the position of the roughness peak $y = h_{max}$.

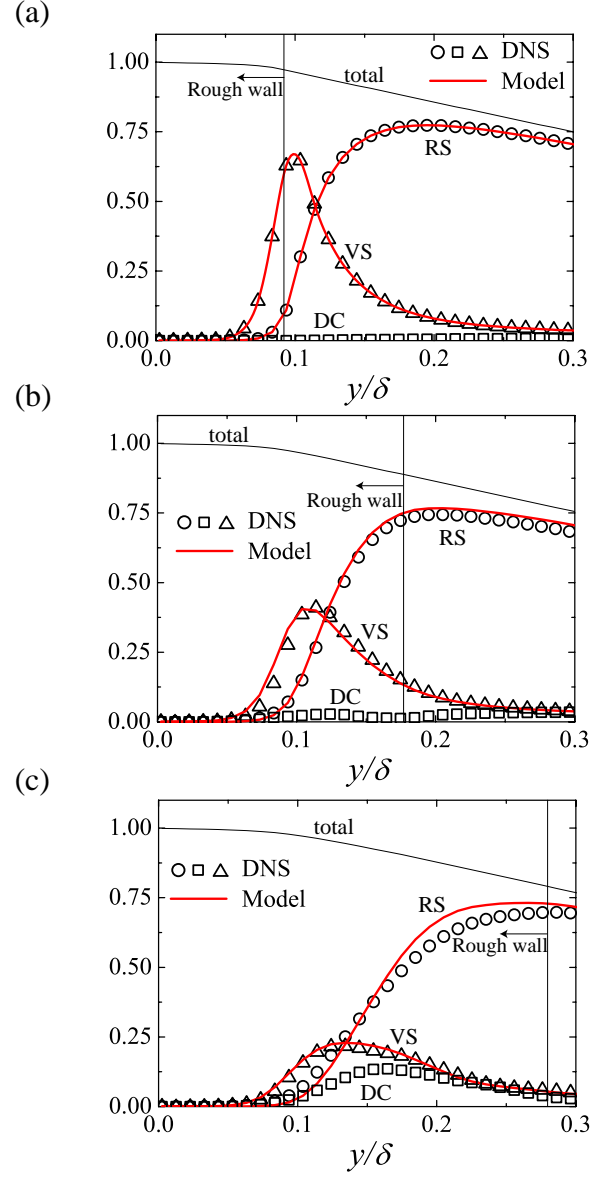


Figure 11: Comparison of the profiles of the plane-averaged Reynolds shear stress, viscous stress, and plane-dispersive covariance: (a) case I, (b) case II, and (c) case III. The vertical solid line indicates the position of the roughness peak $y = h_{max}$.

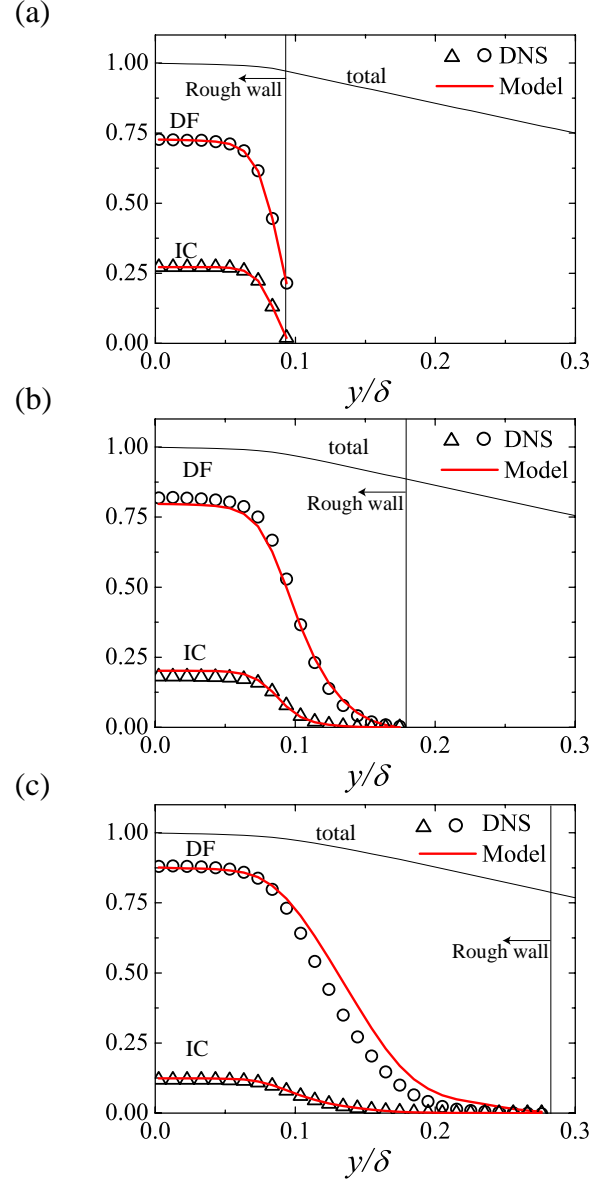


Figure 12: Comparison of the profiles of the plane-averaged drag force and inhomogeneous correction terms: (a) case I, (b) case II, and (c) case III. The vertical solid line indicates the position of the roughness peak $y = h_{max}$.

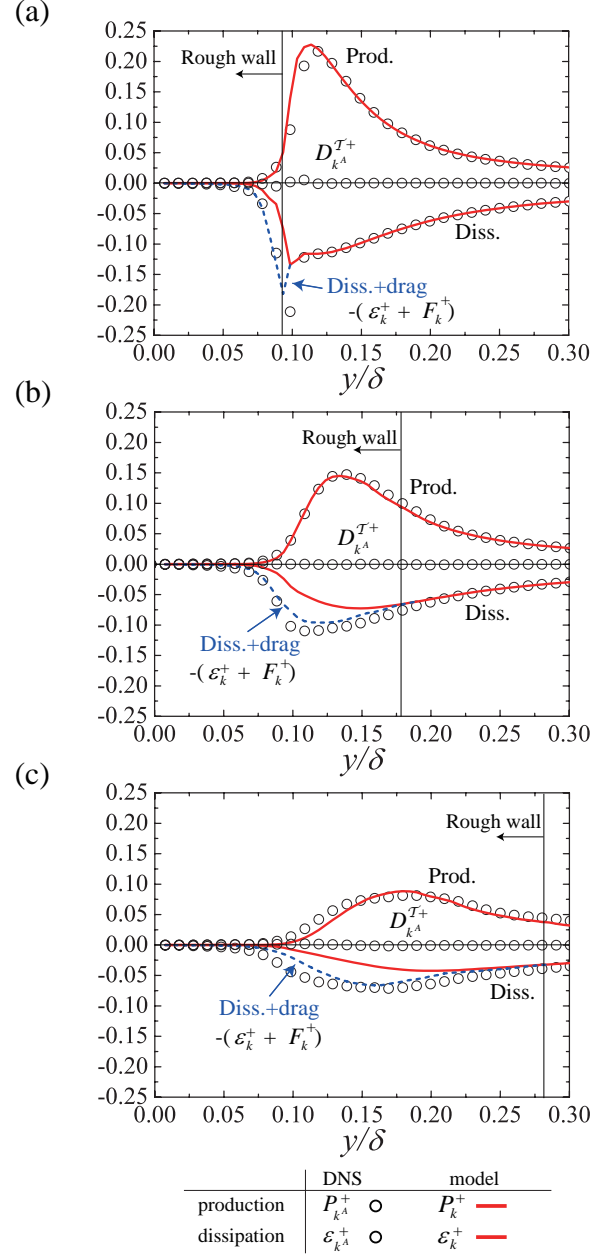


Figure 13: Comparison of the production, dissipation, dispersion transport, and drag force terms in the transport equation of the turbulence energy: (a) case I, (b) case II, and (c) case III. The vertical solid line indicates the position of the roughness peak $y = h_{max}$.

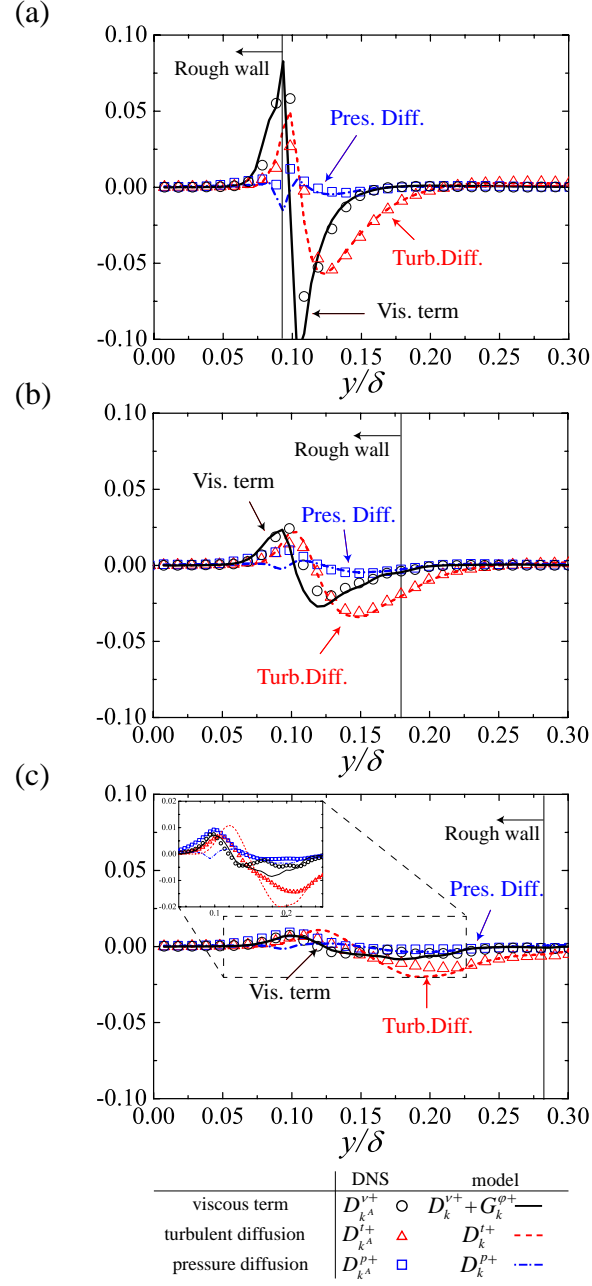


Figure 14: Comparison of the pressure diffusion, turbulent diffusion, and viscous terms in the transport equation of the turbulence energy: (a) case I, (b) case II, and (c) case III. The vertical solid line indicates the position of the roughness peak $y = h_{max}$.

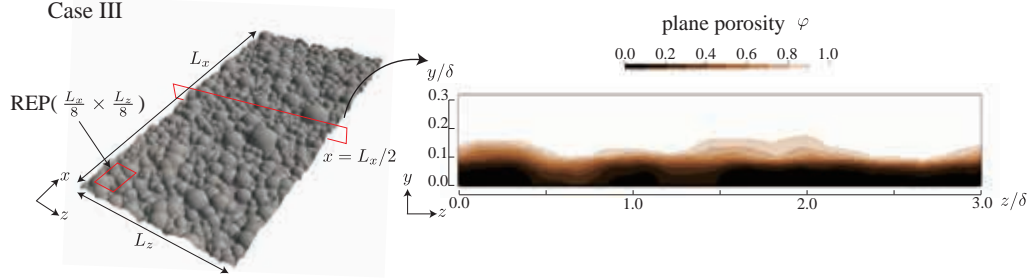


Figure B1: Plane porosity distribution at a center plane of $x/L_x = 0.5$ for case III with the smaller REP size of $\frac{1}{8}L_x(x) \times \frac{1}{8}L_z(z)$

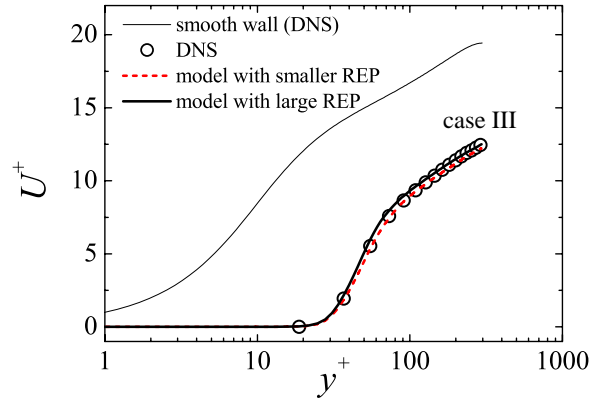


Figure B2: Comparison of the superficial plane-averaged streamwise mean velocity profiles for case III with the different REP size.

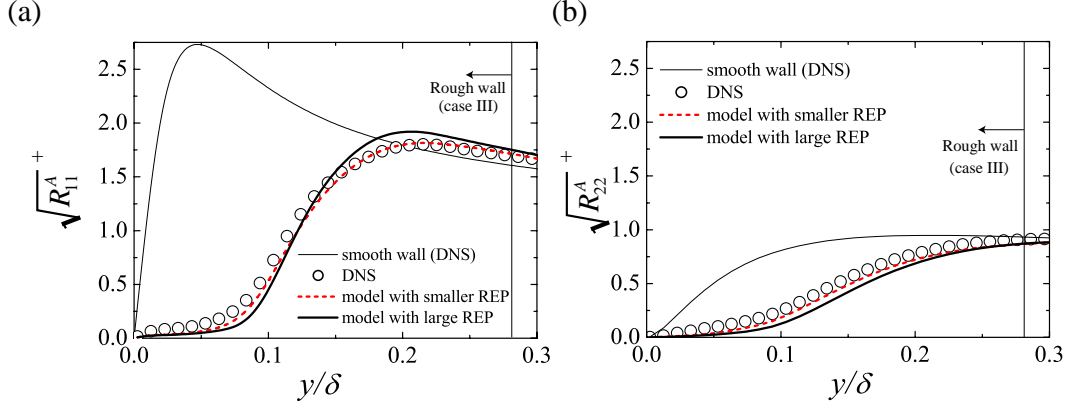


Figure B3: Comparison of the superficial plane-averaged turbulence intensities for case III with the different REP size: (a) streamwise component, (b) wall-normal component. The vertical solid line indicates the position of the roughness peak $y = h_{max}$.

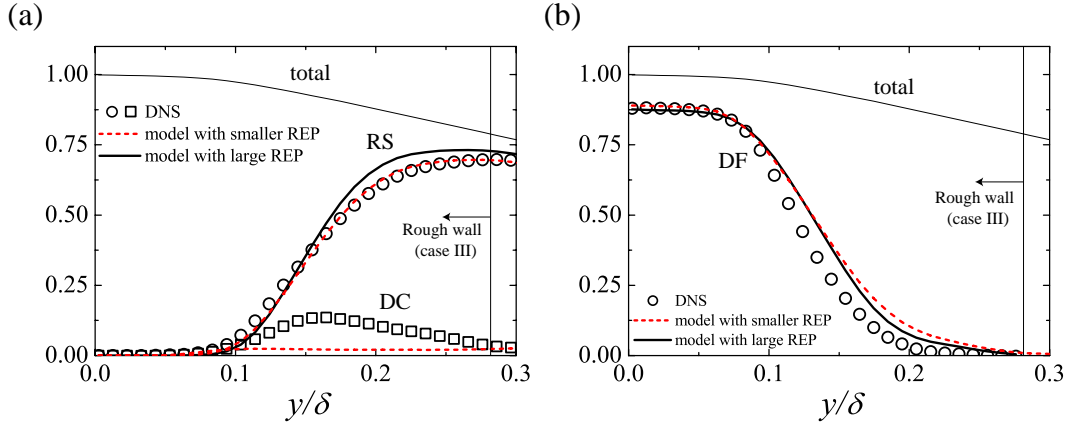


Figure B4: Comparison of the budget terms in the plane-averaged momentum equation for case III with the different REP size: (a) plane-averaged Reynolds shear stress RS and plane-dispersive covariance DC , (b) the plane-averaged drag force term DF . The vertical solid line indicates the position of the roughness peak $y = h_{max}$.

Table 1: Parameters in the D3Q27 discrete velocity model.

Model	c_s/c	ξ_α/c	w_α
D3Q27	$1/\sqrt{3}$	$(0, 0, 0)$	$8/27(\alpha = 0)$
		$(\pm 1, 0, 0), (0, \pm 1, 0), (0, 0, \pm 1)$	$2/27(\alpha = 1, \dots, 6)$
		$(\pm 1, \pm 1, 0), (\pm 1, 0, \pm 1), (0, \pm 1, \pm 1)$	$1/54(\alpha = 7, \dots, 18)$
		$(\pm 1, \pm 1, \pm 1)$	$1/216(\alpha = 19, \dots, 26)$

Table 2: Equilibrium moments.

$m_0^{eq} = \rho \equiv \sum_{\alpha=0}^{26} f_{\alpha}^{eq}$	$m_{13}^{eq} = \psi_x \equiv \frac{9}{2} \sum_{\alpha=0}^{26} (\xi_{\alpha x}^2 + \xi_{\alpha y}^2 + \xi_{\alpha z}^2)^2 \xi_{\alpha x} f_{\alpha}^{eq}$
$m_1^{eq} = j_x \equiv \sum_{\alpha=0}^{26} f_{\alpha}^{eq} \xi_{\alpha x}$	$m_{14}^{eq} = \psi_y \equiv \frac{9}{2} \sum_{\alpha=0}^{26} (\xi_{\alpha x}^2 + \xi_{\alpha y}^2 + \xi_{\alpha z}^2)^2 \xi_{\alpha y} f_{\alpha}^{eq}$
$m_2^{eq} = j_y \equiv \sum_{\alpha=0}^{26} f_{\alpha}^{eq} \xi_{\alpha y}$	$m_{15}^{eq} = \psi_z \equiv \frac{9}{2} \sum_{\alpha=0}^{26} (\xi_{\alpha x}^2 + \xi_{\alpha y}^2 + \xi_{\alpha z}^2)^2 \xi_{\alpha z} f_{\alpha}^{eq}$
$m_3^{eq} = j_z \equiv \sum_{\alpha=0}^{26} f_{\alpha}^{eq} \xi_{\alpha z}$	$m_{16}^{eq} = \varepsilon \equiv \frac{3}{2} \sum_{\alpha=0}^{26} (\xi_{\alpha x}^2 + \xi_{\alpha y}^2 + \xi_{\alpha z}^2)^2 f_{\alpha}^{eq}$
$m_4^{eq} = e \equiv \sum_{\alpha=0}^{26} (\xi_{\alpha x}^2 + \xi_{\alpha y}^2 + \xi_{\alpha z}^2) f_{\alpha}^{eq}$	$m_{17}^{eq} = e_3 \equiv \frac{9}{2} \sum_{\alpha=0}^{26} (\xi_{\alpha x}^2 + \xi_{\alpha y}^2 + \xi_{\alpha z}^2)^3 f_{\alpha}^{eq}$
$m_5^{eq} = XX \equiv \sum_{\alpha=0}^{26} (2\xi_{\alpha x}^2 - \xi_{\alpha y}^2 - \xi_{\alpha z}^2) f_{\alpha}^{eq}$	$m_{18}^{eq} = XX_e \equiv 3 \sum_{\alpha=0}^{26} (2\xi_{\alpha x}^2 - \xi_{\alpha y}^2 - \xi_{\alpha z}^2) (\xi_{\alpha x}^2 + \xi_{\alpha y}^2 + \xi_{\alpha z}^2) f_{\alpha}^{eq}$
$m_6^{eq} = WW \equiv \sum_{\alpha=0}^{26} (\xi_{\alpha y}^2 - \xi_{\alpha z}^2) f_{\alpha}^{eq}$	$m_{19}^{eq} = WW_e \equiv 3 \sum_{\alpha=0}^{26} (\xi_{\alpha y}^2 - \xi_{\alpha z}^2) (\xi_{\alpha x}^2 + \xi_{\alpha y}^2 + \xi_{\alpha z}^2) f_{\alpha}^{eq}$
$m_7^{eq} = XY \equiv \sum_{\alpha=0}^{26} (\xi_{\alpha x} \xi_{\alpha y}) f_{\alpha}^{eq}$	$m_{20}^{eq} = XY_e \equiv 3 \sum_{\alpha=0}^{26} (\xi_{\alpha x} \xi_{\alpha y}) (\xi_{\alpha x}^2 + \xi_{\alpha y}^2 + \xi_{\alpha z}^2) f_{\alpha}^{eq}$
$m_8^{eq} = YZ \equiv \sum_{\alpha=0}^{26} (\xi_{\alpha y} \xi_{\alpha z}) f_{\alpha}^{eq}$	$m_{21}^{eq} = YZ_e \equiv 3 \sum_{\alpha=0}^{26} (\xi_{\alpha y} \xi_{\alpha z}) (\xi_{\alpha x}^2 + \xi_{\alpha y}^2 + \xi_{\alpha z}^2) f_{\alpha}^{eq}$
$m_9^{eq} = ZX \equiv \sum_{\alpha=0}^{26} (\xi_{\alpha z} \xi_{\alpha x}) f_{\alpha}^{eq}$	$m_{22}^{eq} = ZX_e \equiv 3 \sum_{\alpha=0}^{26} (\xi_{\alpha z} \xi_{\alpha x}) (\xi_{\alpha x}^2 + \xi_{\alpha y}^2 + \xi_{\alpha z}^2) f_{\alpha}^{eq}$
$m_{10}^{eq} = \varphi_x \equiv 3 \sum_{\alpha=0}^{26} (\xi_{\alpha x}^2 + \xi_{\alpha y}^2 + \xi_{\alpha z}^2) \xi_{\alpha x} f_{\alpha}^{eq}$	$m_{23}^{eq} = \tau_x \equiv \sum_{\alpha=0}^{26} \xi_{\alpha x} (\xi_{\alpha y}^2 - \xi_{\alpha z}^2) f_{\alpha}^{eq}$
$m_{11}^{eq} = \varphi_y \equiv 3 \sum_{\alpha=0}^{26} (\xi_{\alpha x}^2 + \xi_{\alpha y}^2 + \xi_{\alpha z}^2) \xi_{\alpha y} f_{\alpha}^{eq}$	$m_{24}^{eq} = \tau_y \equiv \sum_{\alpha=0}^{26} \xi_{\alpha y} (\xi_{\alpha z}^2 - \xi_{\alpha x}^2) f_{\alpha}^{eq}$
$m_{12}^{eq} = \varphi_z \equiv 3 \sum_{\alpha=0}^{26} (\xi_{\alpha x}^2 + \xi_{\alpha y}^2 + \xi_{\alpha z}^2) \xi_{\alpha z} f_{\alpha}^{eq}$	$m_{25}^{eq} = \tau_z \equiv \sum_{\alpha=0}^{26} \xi_{\alpha z} (\xi_{\alpha x}^2 - \xi_{\alpha y}^2) f_{\alpha}^{eq}$
	$m_{26}^{eq} = XYZ \equiv \sum_{\alpha=0}^{26} (\xi_{\alpha x} \xi_{\alpha y} \xi_{\alpha z}) f_{\alpha}^{eq}$

ρ : density, j_x, j_y, j_z : momentum, e : kinetic energy, XX, WW, XY, YZ, ZX
 : second-order tensors, $\varphi_x, \varphi_y, \varphi_z$: energy flux, ψ_x, ψ_y, ψ_z : square of the
 energy flux, ε : square of the energy, e_3 : cube of the energy, XX_e, WW_e
 : product of XX and WW by the energy, XY_e, YZ_e, ZX_e : extra-diagonal
 second-order moments of energy, τ_x, τ_y, τ_z : third-order pseudo vector, XYZ
 : third-order totally antisymmetric tensor.

Table 3: 27×27 transformation matrix.

[illegible]

Table 4: Rough wall characteristics and parameters.

Case	h_m/δ	h_{rms}^+	Sk	h_{max}/δ	N_s
I	0.072	7.8	-1.7	0.095	1,650
II	0.079	9.8	-0.73	0.18	1,600
III	0.094	14	0.21	0.28	1,450

Table 5: Flow characteristics of turbulence over rough walls.

Case	C_f	ΔU^+	Re_b	$(C_f^{DNS} - C_f^{model})/C_f^{DNS}$
smooth	0.0070	—	10500	
I(DNS)	0.0113	3.5	7970	—
I(Model)	0.0105	2.9	8280	+7.6%
II (DNS)	0.0145	5.1	7040	—
II(Model)	0.0140	4.8	7180	-3.6%
III(DNS)	0.0201	6.8	5980	—
III(Model)	0.0201	6.8	5980	0.0%

Acknowledgements

The authors express their gratitude to their colleagues: PhD. K. Suga, Dr. M. Kaneda and Dr. T. Tsukahara for their supports. A part of this study was financially supported by the research grants (No.17K14591, 16K14162) of the JSPS Japan. The numerical calculations were carried out on the TSUB-AME2.5 supercomputer in the Tokyo Institute of Technology in research projects (ID: hp170032).

References

- Anderson, W., Barros, J.M., Christensen, K.T., Awasthi, A., 2015. Numerical and experimental study of mechanisms responsible for turbulent secondary flows in boundary layer flows over spanwise heterogeneous roughness. *J. Fluid Mech.* 768, 316–347.
- Ashrafian, A., Andersson, H.I., Manhart, M., 2004. DNS of turbulent flow in a rod-roughened channel. *Int. J. Heat Fluid Flow* 25, 373–383.
- Bespalko, D., Pollard, A., Uddin, M., 2012. Analysis of the pressure fluctuations from an LBM simulation of turbulent channel flow. *Comput. Fluids* 54, 143–146.
- Beugre, D., Calvo, S., Dethier, G., Crine, M., Toye, D., Marchot, P., 2010. Lattice Boltzmann 3D flow simulations on a metallic foam. *J. Comput. Appl. Math.* 234, 2128 – 2134.
- Bhaganagar, K., Kim, J., Coleman, G., 2004. Effect of roughness on wall-bounded turbulence. *Flow Turbulence Combust.* 72, 463–492.

- Bons, J.P., Taylor, R.P., McClain, S.T., Rivir, R.B., 2001. The many faces of turbine surface roughness. *J. Turbomachinery* 123, 739–748.
- Breugem, W., Boersma, B., 2005. Direct numerical simulations of turbulent flow over a permeable wall using a direct and a continuum approach. *Phys. Fluids* 17, 025103.
- Breugem, W.P., Boersma, B.J., Uittenbogaard, R.E., 2006. The influence of wall permeability on turbulent channel flow. *J. Fluid Mech.* 562, 35–72.
- Busse, A., Lutzner, M., Sandham, N.D., 2015. Direct numerical simulation of turbulent flow over a rough surface based on a surface scan. *Comput. Fluids* 116, 129 – 147.
- Busse, A., Sandham, N.D., 2012. Parametric forcing approach to rough-wall turbulent channel flow. *J. Fluid Mech.* 712, 169–202.
- Cardillo, J., Chen, Y., Araya, G., Newman, J., Jansen, K., Castillo, L., 2013. DNS of a turbulent boundary layer with surface roughness. *J. Fluid Mech.* 729, 603–637.
- Chatzikyriakou, D., Buongiorno, J., Caviezel, D., Lakehal, D., 2015. DNS and LES of turbulent flow in a closed channel featuring a pattern of hemispherical roughness elements. *Int. J. Heat Fluid Flow* 53, 29–43.
- Cheng, H., Castro, I.P., 2002. Near wall flow over urban-like roughness. *Boundary Layer Meteorol.* 104, 229–259.
- Chikatamarla, S., Frouzakis, C., Karlin, I., Tomboulides, A., Boulouchos,

- K., 2010. Lattice Boltzmann method for direct numerical simulation of turbulent flows. *J. Fluid Mech.* 656, 298–308.
- Chukwudozie, C., Tyagi, M., 2013. Pore scale inertial flow simulations in 3-D smooth and rough sphere packs using lattice Boltzmann method. *AIChE J.* 59, 4858–4870.
- Colebrook, C.F., Blench, T., Chatley, H., Essex, E., Finniecome, J., Lacey, G., Williamson, J., Macdonald, G., 1939. Correspondence. turbulent flow in pipes, with particular reference to the transition region between the smooth and rough pipe laws.(includes plates). *J. Inst. Civi. Eng.* 12, 393–422.
- Coleman, H., Hodge, B., Taylor, R., 1984. A re-evaluation of schlichting’s surface roughness experiment. *ASME, Transactions, Journal of Fluids Engineering* 106, 60–65.
- d’Humières, D., Ginzburg, I., Krafczyk, M., Lallemand, P., Luo, L.S., 2002. Multiple-relaxation-time lattice Boltzmann models in three dimensions. *Phil. Trans. R. Soc. A* 360, 437–451.
- Dirling, JR, R., 1973. A method for computing roughwall heat transfer rates on reentry nosetips, in: 8th Thermophysics Conference, p. 763.
- Dvorak, F., 1969. Calculation of turbulent boundary layers on rough surfaces in pressure gradient. *AIAA journal* 7, 1752–1759.
- Dwyer, M.J., Patton, E.G., Shaw, R.H., 1997. Turbulent kinetic energy budgets from a large-eddy simulation of airflow above and within a forest canopy. *Boundary-Layer Meteorol.* 84, 23–43.

- Fattahi, E., Waluga, C., Wohlmuth, B., Rde, U., Manhart, M., Helmig, R., 2016. Lattice Boltzmann methods in porous media simulations: From laminar to turbulent flow. *Comput. Fluids* 140, 247–259.
- Finnigan, J., 2000. Turbulence in plant canopies. *Ann. Rev. Fluid Mech.* 32, 519–571.
- Flack, K., Schultz, M., Connelly, J., 2007. Examination of a critical roughness height for outer layer similarity. *Phys. Fluids* 19, 095104.
- Flack, K.A., Schultz, M.P., 2010. Review of hydraulic roughness scales in the fully rough regime. *J. Fluids Engrg.* 132, 041203.
- Flores, O., Jimenez, J., 2006. Effect of wall-boundary disturbances on turbulent channel flows. *J. Fluid Mech.* 566, 357–376.
- Gehrke, M., Janßen, C., Rung, T., 2017. Scrutinizing lattice boltzmann methods for direct numerical simulations of turbulent channel flows. *Comput. Fluids* 156, 247–263.
- Guo, Z., Zheng, C., Shi, B., 2002. Discrete lattice effects on the forcing term in the lattice Boltzmann method. *Phys. Rev. E* 65, 046308.
- Hama, F.R., 1954. Boundary layer characteristics for smooth and rough surfaces. *Trans. Soc. Nav. Arch. Marine Engrs.* 62, 333–358.
- Hasert, M., Bernsdorf, J., Roller, S., 2011. Lattice Boltzmann simulation of non-Darcy flow in porous media. *Procedia Computer Science* 4, 1048–1057.
- Hatiboglu, C.U., Babadagli, T., 2008. Pore-scale studies of spontaneous imbibition into oil-saturated porous media. *Phys. Rev. E* 77, 066311.

- He, X., Luo, L.S., 1997. Lattice Boltzmann model for the incompressible Navier-Stokes equation. *J. Stat. Phys.* 88, 927–944.
- Ikeda, T., Durbin, P.A., 2007. Direct simulations of a rough-wall channel flow. *J. Fluid Mech.* 571, 235–263.
- Jäger, W., Mikelić, A., 2001. On the roughness-induced effective boundary conditions for an incompressible viscous flow. *J. Differential Equations* 170, 96–122.
- Jin, Y., Uth, M., Herwig, H., 2015. Structure of a turbulent flow through plane channels with smooth and rough walls: An analysis based on high resolution DNS results. *Comput. Fluids* 107, 77–88.
- Kim, J., Moin, P., Moser, R., 1987. Turbulence statistics in fully developed channel flow at low Reynolds number. *J. Fluid Mech.* 177, 133–166.
- Kirschner, C.M., Brennan, A.B., 2012. Bio-inspired antifouling strategies. *Annual review of materials research* 42, 211–229.
- Krafczyk, M., Kucher, K., Wang, Y., Geier, M., 2015. DNS/LES studies of turbulent flows based on the cumulant lattice Boltzmann approach, in: *High Performance Computing in Science and Engineering e14*. Springer, pp. 519–531.
- Krogstad, P.Å., Andersson, H., Bakken, O., Ashrafian, A., 2005. An experimental and numerical study of channel flow with rough walls. *J. Fluid Mech.* 530, 327–352.

- Kuwata, Y., Kawaguchi, Y., 2018. Statistical discussions on skin frictional drag of turbulence over randomly distributed semi-spheres. *Int. J. Adv. Engrg. Sci. Appl. Mat.* 10, 263–272.
- Kuwata, Y., Suga, K., 2013. Modelling turbulence around and inside porous media based on the second moment closure. *Int. J. Heat Fluid Flow* 43, 35 – 51.
- Kuwata, Y., Suga, K., 2015a. Anomaly of the lattice Boltzmann methods in three-dimensional cylindrical flows. *J. Comput. Phys.* 280, 563 – 569.
- Kuwata, Y., Suga, K., 2015b. Large eddy simulations of pore-scale turbulent flows in porous media by the lattice Boltzmann method. *Int. J. Heat Fluid Flow* 55, 143–157.
- Kuwata, Y., Suga, K., 2015c. Progress in the extension of a second-moment closure for turbulent environmental flows. *Int. J. Heat Fluid Flow* 51, 268–284.
- Kuwata, Y., Suga, K., 2016a. Imbalance-correction grid-refinement method for lattice Boltzmann flow simulations. *J. Comput. Phys.* 311, 348–362.
- Kuwata, Y., Suga, K., 2016b. Lattice boltzmann direct numerical simulation of interface turbulence over porous and rough walls. *Int. J. Heat Fluid Flow* 61, 145–157.
- Kuwata, Y., Suga, K., 2016c. Transport mechanism of interface turbulence over porous and rough walls. *Flow, Turb. Combust.* 97, 1071–1093.

- Kuwata, Y., Suga, K., 2017. Direct numerical simulation of turbulence over anisotropic porous media. *J. Fluid Mech.* 831, 41–71.
- Kuwata, Y., Suga, K., Sakurai, Y., 2014. Development and application of a multi-scale $k - \varepsilon$ model for turbulent porous medium flows. *Int. J. Heat Fluid Flow* 49, 135–150.
- Lammers, P., Beronov, K.N., Volkert, R., Brenner, G., Durst, F., 2006. Lattice BGK direct numerical simulation of fully developed turbulence in incompressible plane channel flow. *Comput. Fluids* 35, 1137–1153.
- Langelandsvik, L., Kunkel, G., SMITS, A.J., 2008. Flow in a commercial steel pipe. *J. Fluid Mech.* 595, 323–339.
- Lee, J.H., Sung, H.J., Krogstad, P.Å., 2011. Direct numerical simulation of the turbulent boundary layer over a cube-roughened wall. *J. Fluid Mech.* 669, 397–431.
- Leonardi, S., Orlandi, P., Smalley, R., Djenidi, L., Antonia, R., 2003. Direct numerical simulations of turbulent channel flow with transverse square bars on one wall. *J. Fluid Mech.* 491, 229–238.
- Ligrani, P.M., Moffat, R.J., 1986. Structure of transitionally rough and fully rough turbulent boundary layers. *J. Fluid Mech.* 162, 69–98.
- Macdonald, I., El-Sayed, M., Mow, K., Dullien, F., 1979. Flow through porous media-the ergun equation revisited. *Indust. Engng. Chem. Fund.* 18, 199–208.

- Miyake, Y., Tsujimoto, K., Agata, Y., 2000. A DNS of a turbulent flow in a rough-wall channel using roughness elements model. *JSME Int. J. Series B Fluids Thermal Engrg.* 43, 233–242.
- Miyake, Y., Tsujimoto, K., Nakaji, M., 2001. Direct numerical simulation of rough-wall heat transfer in a turbulent channel flow. *Int. J. Heat Fluid Flow* 22, 237–244.
- Moody, L.F., 1944. Friction factors for pipe flow. *Trans. Asme* 66, 671–684.
- Musker, A., 1980. Universal roughness functions for naturally-occurring surfaces. *Trans. Canadian Soc. Mech. Engrg.* 6, 1–6.
- Napoli, E., Armenio, V., De Marchis, M., 2008. The effect of the slope of irregularly distributed roughness elements on turbulent wall-bounded flows. *J. Fluid Mech.* 613, 385–394.
- Nikuradse, J., 1933. Laws of flow in rough pipes, in: *NACA Technical Memorandum* 1292.
- Orlandi, P., Leonardi, S., 2008. Direct numerical simulation of three-dimensional turbulent rough channels: parameterization and flow physics. *J. Fluid Mech.* 606, 399–415.
- Orlandi, P., Leonardi, S., Tuzi, R., Antonia, R., 2003. Direct numerical simulation of turbulent channel flow with wall velocity disturbances. *Phys. Fluids* 15, 3587–3601.
- Parmigiani, A., Huber, C., Bachmann, O., Chopard, B., 2011. Pore-scale

- mass and reactant transport in multiphase porous media flows. *J. Fluid Mech.* 686, 40–76.
- Pinson, F., Grégoire, O., Simonin, O., 2007. Macroscale turbulence modeling for flows in media laden with solid structures. *Compt. Rendus Mecanique* 335, 13–19.
- Raupach, M.R., 1994. Simplified expressions for vegetation roughness length and zero-plane displacement as functions of canopy height and area index. *Boundary Layer Meteorol.* 71, 211–216.
- Schlichting, H., Gersten, K., Krause, E., Oertel, H., Mayes, K., 1960. *Boundary-layer theory*. volume 7. Springer.
- Scotti, A., 2006. Direct numerical simulation of turbulent channel flows with boundary roughened with virtual sandpaper. *Phys. Fluids* 18, 031701.
- Sigal, A., Danberg, J.E., 1990. New correlation of roughness density effect on the turbulent boundary layer. *AIAA journal* 28, 554–556.
- Suga, K., Kuwata, Y., Takashima, K., Chikasue, R., 2015. A D3Q27 multiple-relaxation-time lattice Boltzmann method for turbulent flows. *Comput. Math. Appl.* 69, 518–529.
- Suga, K., Nishio, Y., 2009. Three dimensional microscopic flow simulation across the interface of a porous wall and clear fluid by the lattice Boltzmann method. *The Open Transp. Phenom. J.* 1, 35–44.
- Suga, K., Tanaka, T., Nishio, Y., Murata, M., 2009. A boundary reconstruc-

- tion scheme for lattice Boltzmann flow simulation in porous media. *Prog. Comput. Fluid Dyn.* 9, 201–207.
- Tóth, G., Jánosi, I.M., 2015. Vorticity generation by rough walls in 2D decaying turbulence. *J. Stat. Phys.* 161, 1508–1518.
- Townsin, R., Byrne, D., Svensen, T., Milne, A., 1981. Estimating the technical and economic penalties of hull and propeller roughness. *Trans. SNAME* 89, 295–318.
- Tuck, E., Kouzoubov, A., 1995. A laminar roughness boundary condition. *J. Fluid Mech.* 300, 59–70.
- Van Rij, J.A., Belnap, B., Ligrani, P., 2002. Analysis and experiments on three-dimensional, irregular surface roughness. *ASME, Transactions, J. Fluids Engrg.* 124, 671–677.
- Wahl, M., 1989. Marine epibiosis. I. fouling and antifouling: some basic aspects. *Marine Ecology Progress Series* 58, 175–189.
- Wang, P., Wang, L.P., Guo, Z., 2016. Comparison of the lattice Boltzmann equation and discrete unified gas-kinetic scheme methods for direct numerical simulation of decaying turbulent flows. *Phys. Rev. E* 94, 043304.
- Watanabe, T., 2004. Large-eddy simulation of coherent turbulence structures associated with scalar ramps over plant canopies. *Boundary-Layer Meteorol.* 112, 307–341.
- Whitaker, S., 1986. Flow in porous media I: A theoretical derivation of Darcy’s law. *Transp. Porous Med.* 1, 3–25.

Whitaker, S., 1996. The Forchheimer equation: A theoretical development.
Transp. Porous Med. 25, 27–61.